

Hydrodynamic effects on the filtered dark matter produced by a first-order phase transition

Siyu Jiang,^{1,*} Fa Peng Huang,^{1,†} and Chong Sheng Li²

¹*MOE Key Laboratory of TianQin Mission,
TianQin Research Center for Gravitational Physics & School of Physics and Astronomy,
Frontiers Science Center for TianQin,
Gravitational Wave Research Center of CNSA,*

Sun Yat-sen University (Zhuhai Campus), Zhuhai 519082, China

²*Center for High Energy Physics, Peking University, Beijing 100871, China*

Abstract

Motivated by current status of dark matter (DM) search, a new type of DM production mechanism is proposed based on the dynamical process of a strong first-order phase transition in the early universe, namely, the filtered DM mechanism. We study the hydrodynamic effects on the DM relic density. By detailed calculations, we demonstrate that the hydrodynamic modes with the corresponding hydrodynamic heating effects play essential roles in determining the DM relic density. The corresponding phase transition gravitational wave could help to probe this new mechanism.

* jiangsy36@mail2.sysu.edu.cn

† Corresponding author. huangfp8@sysu.edu.cn

I. INTRODUCTION

Exploring the microscopic nature of dark matter (DM) [1] is an important goal in the interplay of particle physics and cosmology. Besides the well-studied freeze-out, freeze-in and misalignment DM formation mechanisms, recently a new type of mechanism is proposed that the DM is produced due to a strong first-order phase transition (SFOPT) [2–5]. This mechanism could naturally evade the unitarity constraints to form the heavy DM and be detected by phase transition gravitational wave (GW). Especially, the intriguing filtered DM mechanism proposed in Refs. [2, 3] assumes that the DM candidate particles acquire mass when they enter into the bubbles and they are energetically unfavorable to enter into the broken phase. Thus only an extremely small fraction of DM finally enter into the bubbles and then contribute to the observed DM relic density. This mechanism applies to not only DM model but also baryogenesis [6–12]. In the original work of filtered DM, the hydrodynamic effects in the vicinity of the bubble wall are not considered. For example, the temperature in front of and behind the bubble walls is chosen as the same nucleation temperature. However, the DM density depends on the temperature distribution. Actually, to realize the filtered DM, usually it should be a very SFOPT with a large phase transition strength parameter α , which leads to obvious temperature and velocity differences in front of and behind of the bubble wall. These differences originate from the hydrodynamic effects and can significantly enhance or suppress the DM relic density. We study this hydrodynamic effects with dedicated calculations and find that the DM relic density is sensitive to the hydrodynamic modes and the corresponding heating effects.

In Sec. II, we simply present the analytic estimation for the filtered DM mechanism and clearly show the reason to consider the hydrodynamic effects. The phase transition dynamics including the bubble wall velocity are discussed in Sec. III. In Sec. IV, we show how to calculate hydrodynamic profiles of temperature and velocity for zero-width bubble wall. We present the calculations both for spherical and planar bubble wall. The hydrodynamic effects on analytic DM relic density are also given and we emphasize the accuracy of simple low-velocity approximation in the deflagration mode. In Sec. V we show the temperature and velocity profiles across the bubble wall which has nonzero width. In Sec. VI we solve the Boltzmann equation numerically for bubble wall with finite width to get more accurate results. The results of hydrodynamic effects on DM relic density for four benchmark points

are also given. The phase transition GW signals of the filtered DM are given in Sec. VII. Concise conclusions are given in Sec. VIII.

II. ANALYTIC ESTIMATION

To clearly see that the hydrodynamic effects play important roles in the final DM relic density, we firstly demonstrate simple analytic estimation of the DM density. Then we perform detailed calculation of the DM density explicitly using the Boltzmann equations to include the hydrodynamic effects.

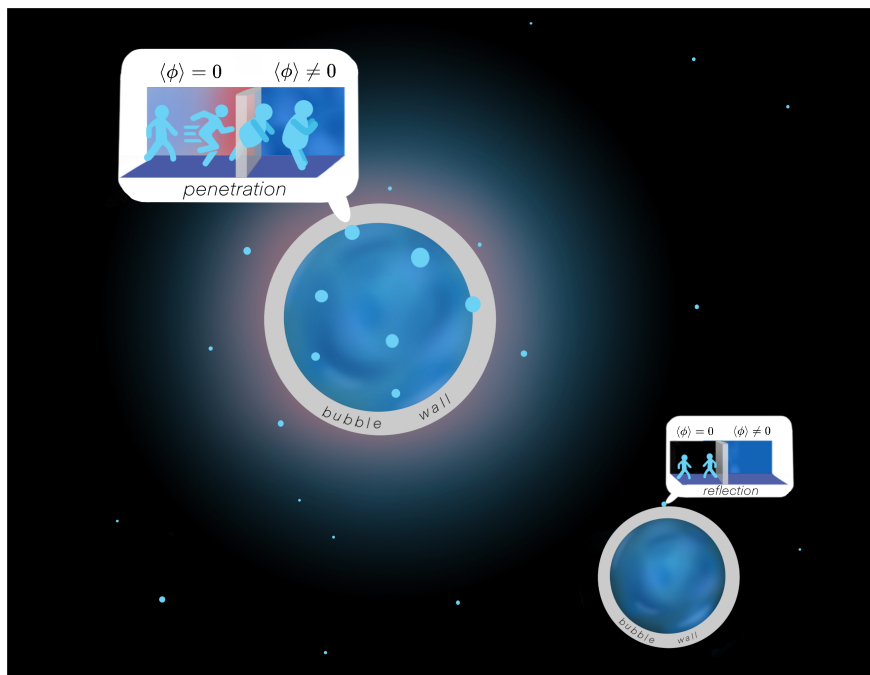


FIG. 1. Schematic process for the filtered DM with hydrodynamic effects for the deflagration mode. In upper left we show that due to the heating effects the DM has more abilities to pass through the bubble wall. In lower right the DM is more likely to reflect by the bubble wall.

In Fig. 1, we show the basic process for the filtered DM with hydrodynamic effects for the deflagration mode. ϕ is the phase transition field during a SFOPT, and bubbles nucleate in the thermal plasma of the early universe. In upper left we show that due to the hydrodynamic effects, the region in front of the bubble wall is heating (red color) and then the DM increase the probability to pass through the bubble wall than one without considering hydrodynamic effects. In lower right the DM is more likely to reflect by the bubble wall. The bubble walls

formed during a SFOPT can provide new approaches to produce heavy DM through the filtering effects. Due to the energy conservation, only a Boltzmann-suppressed fraction of the would-be-DM particles with very large momenta can pass through the bubbles walls and then contribute to the DM relic density when the particles hit the wall. It is straightforward to discuss the filtering effects in the bubble wall frame with the following condition [2, 3],

$$p_z^w > \sqrt{\Delta m^2}, \quad (1)$$

where p_z^w is the particle z -direction momentum in the bubble wall frame, $\Delta m^2 = (m_\chi^{\text{in}})^2 - m_0^2$ with m_χ^{in} the mass of DM particle χ deep inside the bubble wall and m_0 the mass in the false vacuum [8].

Assuming the DM particle χ is in thermal equilibrium outside the bubble, such that in bubble wall frame its distribution function follows the Bose-Einstein or Fermi-Dirac distribution

$$f_\chi^{\text{eq}} = \frac{1}{e^{\tilde{\gamma}_{\text{pl}}(\sqrt{(p^w)^2 + m_0^2} - \tilde{v}_{\text{pl}} p_z^w)/T} \mp 1}, \quad (2)$$

where \tilde{v}_{pl} is the relative velocity of fluid bulk motion with respect to the wall and $\tilde{\gamma}_{\text{pl}} = 1/\sqrt{1 - \tilde{v}_{\text{pl}}^2}$ is its Lorentz factor. $p^w \equiv |\mathbf{p}^w|$ is the magnitude of the three-momentum of DM and T is the temperature of DM. The particle flux coming from the false vacuum per unit area and unit time can be written as [2, 3]

$$J_\chi^w = g_\chi \int \frac{d^3 p^w}{(2\pi)^3} \frac{p_z^w}{E^w} f_\chi^{\text{eq}} \Theta(p_z^w - \sqrt{\Delta m^2}), \quad (3)$$

where g_χ being the DM degrees of freedom. Then the DM number density inside the bubble n_χ^{in} in the bubble center frame can be written as [2, 3]

$$n_\chi^{\text{in}} = \frac{J_\chi^w}{\gamma_w v_w}. \quad (4)$$

where v_w is the bubble wall velocity and $\gamma_w = 1/\sqrt{1 - v_w^2}$ is its Lorentz factor. In our work we set $m_0 = 0$, and then we can integrate Eq. (3) and get [3]

$$n_\chi^{\text{in}} \simeq \frac{g_\chi T^3}{\gamma_w v_w} \left(\frac{\tilde{\gamma}_{\text{pl}} (1 - \tilde{v}_{\text{pl}}) m_\chi^{\text{in}}/T + 1}{4\pi^2 \tilde{\gamma}_{\text{pl}}^3 (1 - \tilde{v}_{\text{pl}})^2} \right) e^{-\frac{\tilde{\gamma}_{\text{pl}}(1 - \tilde{v}_{\text{pl}}) m_\chi^{\text{in}}}{T}}, \quad (5)$$

where we have used Maxwell-Boltzmann approximation of DM distribution. We can see that as $\tilde{v}_{\text{pl}} \rightarrow 1$, $\tilde{\gamma}_{\text{pl}} \gg 1$, by using $\tilde{\gamma}_{\text{pl}} (1 - \tilde{v}_{\text{pl}}) = \tilde{\gamma}_{\text{pl}} - \sqrt{\tilde{\gamma}_{\text{pl}}^2 - 1} \rightarrow \frac{1}{2\tilde{\gamma}_{\text{pl}}}$, the exponent approaches $-m_\chi^{\text{in}}/(2\tilde{\gamma}_{\text{pl}}T)$. On the other hand, in the case of $\tilde{v}_{\text{pl}} \rightarrow 0$, $\tilde{\gamma}_{\text{pl}} \rightarrow 1$ and the exponent becomes

$-m_\chi^{\text{in}}/T$. Then we could find that when $\tilde{\gamma}_{\text{pl}} \gg m_\chi^{\text{in}}/T$, Eq. (5) approaches $g_\chi T^3/\pi^2$ which is the equilibrium number density for Boltzmann distribution outside the bubble. It means that all particles can pass through the bubble wall, i.e., the bubble wall does not filter out DM particles in this limit.

The DM abundance today can be calculated by dividing n_χ^{in} by the entropy density $s = (2\pi^2/45)g_{\star s}(T')T'^3$ inside the bubble, where $g_{\star s}(T')$ is the effective number of relativistic degrees of freedom associated with entropy and T' is the temperature behind the bubble wall. After normalizing to the critical density $\rho_c = 3H_0^2 M_{\text{pl}}^2$ we have [2, 6] :

$$\Omega_{\text{DM}} h^2 = \frac{m_\chi^{\text{in}}(n_\chi^{\text{in}} + n_{\bar{\chi}}^{\text{in}})}{\rho_c/h^2} \frac{g_{\star s0} T_0^3}{g_{\star s}(T') T'^3} \simeq 6.29 \times 10^8 \frac{m_\chi^{\text{in}}}{\text{GeV}} \frac{(n_\chi^{\text{in}} + n_{\bar{\chi}}^{\text{in}})}{g_{\star s}(T') T'^3}. \quad (6)$$

where $T_0 \simeq 0.235$ meV is the temperature today and $g_{\star s0} = 3.9$ is the effective degree of freedom at present. $h = H_0/(100 \text{ km/sec/Mpc}) = 0.678$ [13] is the dimensionless parameter in the observed Hubble constant H_0 .

In the original work of Ref. [2] they do not consider the variation of velocity and temperature across the bubble wall from the hydrodynamic effects, namely, they choose

$$\tilde{v}_{\text{pl}} = v_w, \quad T = T' = T_n \quad \rightarrow \quad \Omega_{\text{DM}}^{(0)} h^2 \text{ [2]} \quad (7)$$

Then we can show the contour plot of the observed DM relic density $\Omega_{\text{DM}}^{(0)} h^2 = 0.12$ in the left panel of Fig. 2. It is shown that we can not generally impose an ultra-relativistic bubble wall with $\gamma_w \gg 1$. For $v_w \rightarrow 0.01$, i.e., $\gamma_w \rightarrow 1$, we have to impose m_χ^{in}/T_n around 40. And for $v_w > 0.9$, i.e., $\gamma_w > 2.3$, we generally have to impose $m_\chi^{\text{in}}/T_n > 100$ to efficiently filter the DM.

We can define the DM penetration rate $R_{\text{in}}^{(0)}$ as in the original works as

$$R_{\text{in}}^{(0)} = \frac{n_\chi^{\text{in}}}{n_\chi^{\text{out}}}, \quad (8)$$

where $n_\chi^{\text{out}} = g_\chi T^3/\pi^2$ is the equilibrium DM number density outside the bubble wall at the time of the phase transition. We show the penetration rate $R_{\text{in}}^{(0)}$ in right panel of Fig. 2. This quantity evaluates the filtering ability of the bubble wall. The larger the $R_{\text{in}}^{(0)}$ is, the weaker the filtering effect is.

Actually, the temperature and velocity are not constants across the bubble wall. As the bubble wall expand, the vacuum energy releases, and then causes reheating and bulk

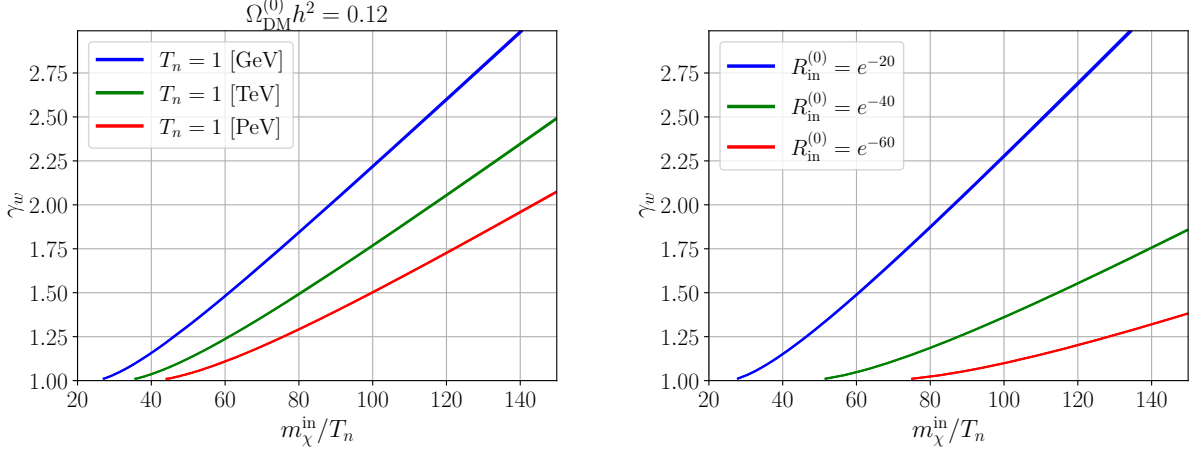


FIG. 2. Left: Contour plot of γ_w and m_χ^{in}/T_n with DM relic density $\Omega_{\text{DM}}^{(0)} h^2 = 0.12$ without hydrodynamic effects. Right: penetration rate $R_{\text{in}}^{(0)}$ as functions of γ_w and m_χ^{in}/T_n without hydrodynamic effects.

motions of the plasma around the bubble wall. We denote the quantities in front of the bubble wall with $+$ and behind the wall with $-$. Then in the filtered DM mechanism, \tilde{v}_{pl} and T in Eq. (2) should be evaluated in front of the bubble wall and T' is the temperature behind the bubble wall,

$$\tilde{v}_{\text{pl}} = \tilde{v}_+, \quad T = T_+, \quad T' = T_- \quad (\text{this work with hydrodynamic effects}) . \quad (9)$$

Then Eq. (5) should be rewritten as

$$n_\chi^{\text{in}} \simeq \frac{g_\chi T_+^3}{\gamma_w v_w} \left(\frac{\tilde{\gamma}_+ (1 - \tilde{v}_+) m_\chi^{\text{in}}/T_+ + 1}{4\pi^2 \tilde{\gamma}_+^3 (1 - \tilde{v}_+)^2} \right) e^{-\frac{\tilde{\gamma}_+ (1 - \tilde{v}_+) m_\chi^{\text{in}}}{T_+}} , \quad (10)$$

and we have DM relic density

$$\Omega_{\text{DM}}^{(\text{hy})} h^2 = \frac{m_\chi^{\text{in}} (n_\chi^{\text{in}} + n_{\bar{\chi}}^{\text{in}})}{\rho_c/h^2} \frac{g_{*s0} T_0^3}{g_{*s}(T_-) T_-^3} \simeq 6.29 \times 10^8 \frac{m_\chi^{\text{in}}}{\text{GeV}} \frac{(n_\chi^{\text{in}} + n_{\bar{\chi}}^{\text{in}})}{g_{*s}(T_-) T_-^3} . \quad (11)$$

This can also be expressed in terms of the renewed penetration rate $R_{\text{in}}^{(\text{hy})}$,

$$\Omega_{\text{DM}}^{(\text{hy})} h^2 = 6.37 \times 10^7 \frac{m_\chi^{\text{in}}}{\text{GeV}} \frac{2g_\chi}{g_{*s}(T_-)} \left(\frac{T_+}{T_-} \right)^3 R_{\text{in}}^{(\text{hy})} . \quad (12)$$

with

$$R_{\text{in}}^{(\text{hy})} = \frac{1}{\gamma_w v_w} \left(\frac{\tilde{\gamma}_+ (1 - \tilde{v}_+) m_\chi^{\text{in}} / T_+ + 1}{4\tilde{\gamma}_+^3 (1 - \tilde{v}_+)^2} \right) e^{-\frac{\tilde{\gamma}_+ (1 - \tilde{v}_+) m_\chi^{\text{in}}}{T_+}}. \quad (13)$$

We generally have two distinct cases: (a) For phase transition with $\alpha_n \lesssim 1$, we expect that T_- will be different with T_+ by a $\mathcal{O}(1)$ factor and the DM relic abundance is dominantly set by filtering effects. (b) However, for strong super-cooling phase transition $\alpha_n \gg 1$, we expect the wall velocity is ultra-relativistic and the dominant mechanism is *super-cool DM* [14] which produce very large T_-/T_+ to suppress the relic density of DM. In the latter case, we still want to quantify the filtering effects in order to get accurate results. We need to evaluate $R_{\text{in}}^{(\text{hy})}$ in a given model.

It is obviously important to evaluate the temperature and velocity in front of and behind the bubble wall. On one hand, as the typical energy of DM in front of the bubble wall is proportional to the temperature T_+ , higher temperature T_+ in front of the bubble wall means stronger ability of DM to pass through the bubble wall. However, larger T_- may lead to larger vacuum value behind the wall then larger m_χ^{in} . This make it harder for DM to pass through the bubble wall. On the other hand, the velocity determines the momentum distribution of DM which affects the DM number density. The heating effects are firstly mentioned by Ref. [3] without calculations. In this work we demonstrate how to calculate the hydrodynamic effects in details.

III. PHASE TRANSITION DYNAMICS

A. toy model

To work in the filtered DM mechanism, we assume the DM model

$$\mathcal{L} = -y_\chi \bar{\chi} \Phi \chi - V(\Phi) - \kappa \Phi^\dagger \Phi H^\dagger H + h.c. , \quad (14)$$

where Φ is a scalar doublet and $V(\Phi)$ is the tree-level potential of Φ . χ is a Dirac particle which would be the DM candidate. This model can represent a variety of phase transition models like the inert scalar models. The mixing term $\kappa \Phi^\dagger \Phi H^\dagger H$ behaves as a portal with which the DM can become thermal equilibrium with SM plasma outside the bubble wall then they share the same temperature and velocity. And due to this portal coupling ϕ can annihilate away after phase transition.

The background field is defined as

$$\Phi = (0, \phi/\sqrt{2})^T . \quad (15)$$

We assume the effective scalar potential at finite temperature is of the form

$$V_{\text{eff}}(\phi, T) = \frac{\mu^2 + DT^2}{2} \phi^2 - CT\phi^3 + \frac{\lambda}{4} \phi^4 - \frac{g_* \pi^2 T^4}{90}, \quad (16)$$

Where $g_* = g_{*s}$ is the effective number of freedom. We choose $g_* = 120$ for simplicity as counting some extra particle species.

The critical temperature is

$$T_c = \frac{2}{\lambda D - 2C^2} \left[\frac{\sqrt{\lambda D (\lambda D - 2C^2)} T_b^2}{2} \right], \quad (17)$$

where

$$T_b^2 = -\frac{\mu^2}{D} = \frac{\lambda}{D} v_0^2, \quad (18)$$

is the temperature when the potential barrier vanishes. We choose zero-temperature vacuum value $v_0 = 246$ GeV. The two minima are

$$\langle \phi \rangle = 0, \quad \frac{3CT}{2\lambda} \left[1 + \sqrt{1 - \frac{4\lambda(\mu^2 + DT^2)}{9C^2 T^2}} \right] \equiv \phi_T. \quad (19)$$

We then have DM mass inside the bubble wall,

$$m_\chi^{\text{in}} = \frac{y_\chi \phi_-}{\sqrt{2}}, \quad (20)$$

where $\phi_- = \phi(T_-)$ is the field value which is evaluated at the temperature behind the bubble wall.

We use *CosmoTransitions* [15] to find the phase transition points. The bubbles begin to nucleate when bounce action $S_3(T_n)/T_n \simeq 142$. Actually, this simple potential has semi-analytical approximation for the tunneling action [16, 17]

$$\frac{S_3}{T} = \frac{C}{\lambda^{3/2}} \frac{64\pi\sqrt{\delta}(\beta_1\delta + \beta_2\delta^2 + \beta_3\delta^3)}{81(2 - \delta)^2} \quad (21)$$

with

$$\delta = \frac{\lambda(\mu^2 + DT^2)}{C^2 T^2}. \quad (22)$$

and $\beta_1 = 8.2938$, $\beta_2 = -5.5330$, $\beta_3 = 0.8180$.

	D	C	λ	T_n [GeV]	α_n	β/H	ϕ_n/T_n
BP_1	0.4	0.04	0.01	45.13	0.23	1531.69	11
BP_2	0.3	0.036	0.01	53.42	0.13	1299.67	10
BP_3	0.5	0.04	0.01	39.03	0.31	2044.65	11.1
BP_4	0.7	0.055	0.01	33.6	0.81	1659.02	15.4

TABLE I. Four sets of benchmark model parameters.

Then we use the following definition of the phase transition strength,

$$\alpha \equiv \frac{\left(1 - \frac{T}{4} \frac{\partial}{\partial T}\right) \Delta V_{\text{eff}}}{\pi^2 g_* T^4 / 30}, \quad (23)$$

where ΔV_{eff} is the potential difference between the false and true vacuum. We have also the inverse duration of the phase transition

$$\beta = -\frac{d}{dt} \frac{S_3(T)}{T} = H(T) T \frac{d}{dT} \frac{S_3(T)}{T}. \quad (24)$$

We can also have the analytic expression of α and β which has shown in Appendix. A. In Appendix. A we also show that the analytical expression and CosmoTransitions give almost the same results. We show four benchmark points in Tab. I. In our work we mainly work in BP_1 and we also show the results of other three benchmark points. We also use the semi-analytic method to scan the parameters in toy model as shown in Fig. 3. We fix $\lambda = 0.01$ and we show four phase-transition parameters T_n , α_n , ϕ_n/T_n and β/H_n as functions of D , C in the toy model.

B. bubble wall velocity

Precise calculation of bubble wall velocity is still difficult now. In reality, this should be done by evaluating the interactions between the bubble and the plasma. The friction comes from the non-equilibrium part of heavy particles that have masses comparable with the phase transition temperature. The solution of bubble wall velocity requires us to solve the EOM including non-equilibrium part [18–20]

$$\partial^2 \phi + \frac{\partial V_{\text{eff}}}{\partial \phi} = \sum_{i=\text{B,F}} g_i \frac{dm_i^2}{d\phi} \int \frac{d^3 p}{(2\pi)^3} \frac{\delta f_i}{2E_i} \quad (25)$$

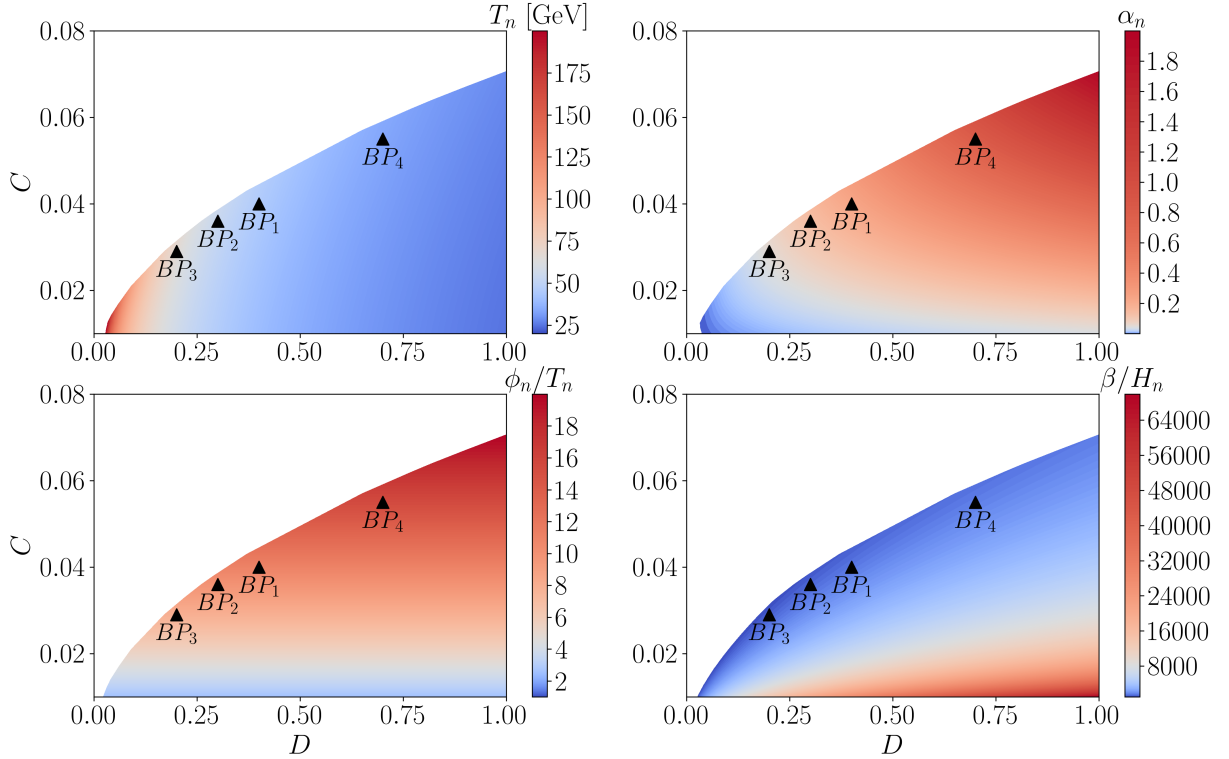


FIG. 3. Scan of the parameters in the toy model with fixed $\lambda = 0.01$. We show the four phase-transition parameters T_n , α_n , ϕ_n/T_n and β/H_n . $H_n = H(T_n)$ is the Hubble expansion rate at nucleation temperature T_n .

However, even in local equilibrium, there is still an effective friction on bubble wall [21–23]. The general quantum field theoretic formula shows that [21]

$$\Delta P_{\text{e}} = (\gamma_w^2 - 1)T\Delta s \quad (26)$$

For ultra-relativistic bubble wall with $\gamma_w T_n \gg m_i$ the leading order contribution of friction is [24]

$$\Delta P_{\text{LO}} = \sum_i g_i c_i \frac{\Delta m_i^2}{24} T_n^2, \quad (27)$$

where g_i is the number of freedom of the particles and $\Delta m_i^2 = m_i^2(\phi_-) - m_i^2(\phi_+)$ with ϕ_- and ϕ_+ are the vacuum value behind and in front of the bubble wall, respectively. $c_i = 1$ for bosons and $c_i = 1/2$ for fermions.

For ultra-relativistic bubble wall the next-to-leading-order friction can be expressed as follow, proportional to γ_w [25]

$$\Delta P_{\text{NLO}}^{(1)} \approx \gamma_w \sum_{j \in V} \lambda_j m_j T_n^3 \log \frac{m_j}{\mu_{ref}} , \quad (28)$$

where $\sum_{j \in V}$ sums over only gauge bosons and λ_j is their gauge couplings. $\mu_{ref} \approx \lambda_j T_n$ is an IR cutoff.

Ref. [26] reports another expression for the NLO friction:

$$\Delta P_{\text{NLO}}^{(2)} \approx \gamma_w^2 \sum_{j \in V} \lambda_j g_j T_n^4 . \quad (29)$$

In Ref. [3], they pointed that for filtered DM mechanism the main friction should come from the heavy particles :

$$\Delta P_{\text{heavy}} = \frac{d_n g_\star \pi^2}{90} (1 + v_w)^3 \gamma_w^2 T_n^4 , \quad (30)$$

where

$$d_n \equiv \frac{1}{g_\star} \left[\sum_{0.2m_i > \gamma_w T_n} \left(g_i^b + \frac{7}{8} g_i^f \right) \right] , \quad (31)$$

with g_i^b and g_i^f , the number of degrees of freedom of the bosons and fermions, respectively. This has similar form as Eq. (26). For heavy particles in false vacuum they have entropy density $s \propto T^3$ and in true vacuum their contribution to entropy density is approximately zero.

In this work, we focus on the hydrodynamic effects on the DM relic density. And the bubble wall velocity is an important parameter to determine the hydrodynamic mode. To obtain more general results, we do not specify the definite bubble wall velocity, but discuss three hydrodynamic modes for different bubble wall velocities.

IV. VELOCITY AND TEMPERATURE DISTRIBUTION FROM HYDRODYNAMIC EFFECTS WITH ZERO-WIDTH BUBBLE WALL

As the bubble wall is expanding, the phase transition happens and the latent heat is injected, which causes reheating and bulk motions of the plasma. This produces the temperature and velocity profiles around the bubble wall. In this section we discuss the hydrodynamic effects without considering the thickness of the bubble wall [27].

A. continuity equations

The energy-momentum tensor (EMT) for scalar field ϕ is

$$T_{\phi}^{\mu\nu} = \partial^{\mu}\phi\partial^{\nu}\phi - g^{\mu\nu} \left[\frac{1}{2}\partial_{\alpha}\phi\partial^{\alpha}\phi - V_{T=0}(\phi) \right], \quad (32)$$

where $V_{T=0}(\phi)$ is the effective potential at zero temperature which includes one-loop quantum corrections.

The energy-momentum tensor for plasma is

$$T_{\text{pl}}^{\mu\nu} = \sum_i \int \frac{d^3k}{(2\pi)^3 E_i} k^{\mu} k^{\nu} f_i^{\text{eq}}(k), \quad (33)$$

which can be parameterized as a perfect fluid

$$T_{\text{pl}}^{\mu\nu} = \omega_{\text{pl}} u_{\text{pl}}^{\mu} u_{\text{pl}}^{\nu} - p_{\text{pl}} g^{\mu\nu}, \quad (34)$$

where $u_{\text{pl}}^{\mu} = (\gamma, \gamma\vec{v})$ with $\gamma = 1/\sqrt{1-v^2}$ in the frame of the bubble center, the thermal pressure p_{pl} and enthalpy ω_{pl} are

$$p_{\text{pl}} = \pm T \sum_i \int \frac{d^3k}{(2\pi)^3} \log [1 \pm \exp(-E_i/T)], \quad (35)$$

$$\omega_{\text{pl}} = T \frac{\partial p_{\text{pl}}}{\partial T} = e_{\text{pl}} + p_{\text{pl}},$$

with $E_i = \sqrt{k^2 + m_i^2}$ defined in the plasma rest frame. The signs $+/-$ denote fermions/bosons.

Because for scalar field EMT we have $\omega_{\phi} = e_{\phi} + p_{\phi} = 0$ and $p_{\phi} = -V_{T=0}(\phi)$, we can write the EMT of the total system as

$$T_{\text{fl}}^{\mu\nu} = T_{\phi}^{\mu\nu} + T_{\text{pl}}^{\mu\nu} = \omega u^{\mu} u^{\nu} - p g^{\mu\nu}, \quad (36)$$

with $\omega = \omega_{\text{pl}}$, $u^{\mu} = u_{\text{pl}}^{\mu}$ and $p = p_{\text{pl}} - V_{T=0}$.

We can parameterize the equation of state by using the bag model. In the false vacuum,

$$p_{+} = \frac{1}{3} a_{+} T_{+}^4 - \epsilon, \quad e_{+} = a_{+} T_{+}^4 + \epsilon. \quad (37)$$

In the broken phase

$$p_{-} = \frac{1}{3} a_{-} T_{-}^4, \quad e_{-} = a_{-} T_{-}^4. \quad (38)$$

Here

$$a_{\pm} \equiv \frac{3}{4T_{\pm}^3} \frac{\partial p}{\partial T} \Big|_{\pm} = \frac{3\omega_{\pm}}{4T_{\pm}^4}, \quad \epsilon_{\pm} = \frac{1}{4} (e_{\pm} - 3p_{\pm}), \quad (39)$$

where a_{\pm} are the number of freedom in the true and false vacuum respectively. Mostly $a_+ > a_-$ as counting the heavy particles across the bubble wall. ϵ denotes the false-vacuum energy which is often defined to be zero in the broken, true-minimum phase.

We consider the continuity equations which come from the energy-momentum conservation,

$$\nabla_{\mu} T^{\mu\nu} = u^{\nu} \nabla_{\mu} (u^{\mu} \omega) + u^{\mu} \omega \nabla_{\mu} u^{\nu} - \nabla^{\nu} p = 0 . \quad (40)$$

Project along the direction of the flow of the fluid, and use $u_{\mu} \partial_{\nu} u^{\mu} = 0$, we get

$$\nabla_{\mu} (u^{\mu} \omega) - u_{\mu} \nabla^{\mu} p = 0 . \quad (41)$$

Next project perpendicular to the flow with some space-like vector $\bar{u} = \gamma(v, \mathbf{v}/v)$ such that $\bar{u}_{\mu} u^{\mu} = 0, \bar{u}^2 = -1$. Then we have

$$\bar{u}^{\nu} u^{\mu} \omega \nabla_{\mu} u_{\nu} - \bar{u}^{\nu} \nabla_{\nu} p = 0 . \quad (42)$$

Since there is no characteristic distance scale in the problem, the solution could be described by a self-similar parameter $\xi = r/t$ where r is the distance from the bubble center and t the time from nucleation. Then the gradients will be turned into

$$u_{\mu} \nabla^{\mu} = -\frac{\gamma}{t} (\xi - v) \partial_{\xi}, \quad \bar{u}_{\mu} \nabla^{\mu} = \frac{\gamma}{t} (1 - \xi v) \partial_{\xi} . \quad (43)$$

By using

$$\nabla_{\mu} u^{\mu} = \frac{jv}{\xi} \frac{\gamma}{t} + \frac{\gamma}{t} \gamma^2 (1 - \xi v) \partial_{\xi} v , \quad (44)$$

with $j = 0, 1, 2$ for planar, cylindrical and spherical cases, respectively. Then Eqs. (41) and (42) can be transformed into

$$\begin{aligned} (\xi - v) \frac{\partial_{\xi} e}{\omega} &= j \frac{v}{\xi} + [1 - \gamma^2 v (\xi - v)] \partial_{\xi} v , \\ (1 - v\xi) \frac{\partial_{\xi} p}{\omega} &= \gamma^2 (\xi - v) \partial_{\xi} v . \end{aligned} \quad (45)$$

The derivatives $\partial_{\xi} e$ and $\partial_{\xi} p$ can be related through the speed of sound in the plasma, $c_s^2 \equiv (dp/dT)/(de/dT)$, then from Eq. (45) we have

$$\begin{aligned} j \frac{v}{\xi} &= \gamma^2 (1 - v\xi) \left[\frac{\mu^2}{c_s^2} - 1 \right] \partial_{\xi} v , \\ \frac{\partial_{\xi} \omega}{\omega} &= \left(1 + \frac{1}{c_s^2} \right) \gamma^2 \mu \partial_{\xi} v . \end{aligned} \quad (46)$$

with μ the Lorentz-transformed fluid velocity

$$\mu(\xi, v) = \frac{\xi - v}{1 - \xi v}. \quad (47)$$

In many cases c_s^2 only slightly deviates from $1/3$. After getting $v(\xi)$, we can integrate Eq. (46),

$$\omega(\xi) = \omega_0 \exp \left[\int_{v_0}^{v(\xi)} \left(1 + \frac{1}{c_s^2} \right) \gamma^2 \mu dv \right] \quad (48)$$

B. matching conditions

In order to solve the continuity equations, we must impose some boundary conditions. There is two boundary in our cases, the bubble wall which is at $\xi_w = v_w$ and the shock front ξ_{sh} . In the reference frame of the bubble wall, we can again use the energy-momentum conservation across the boundary, remember that we denote \tilde{v} as velocity in the frame of the bubble wall

$$\omega_+ \tilde{v}_+^2 \tilde{\gamma}_+^2 + p_+ = \omega_- \tilde{v}_-^2 \tilde{\gamma}_-^2 + p_-, \quad \omega_+ \tilde{v}_+ \tilde{\gamma}_+^2 = \omega_- \tilde{v}_- \tilde{\gamma}_-^2. \quad (49)$$

From these equations we can obtain the relations

$$\tilde{v}_+ \tilde{v}_- = \frac{p_+ - p_-}{e_+ - e_-} = \frac{1 - (1 - 3\alpha_+) r_\omega}{3 - 3(1 + \alpha_+) r_\omega}, \quad \frac{\tilde{v}_+}{\tilde{v}_-} = \frac{e_- + p_+}{e_+ + p_-} = \frac{3 + (1 - 3\alpha_+) r_\omega}{1 + 3(1 + \alpha_+) r_\omega}. \quad (50)$$

with $\alpha_+ \equiv \epsilon / (a_+ T_+^4)$ and $r_\omega = \omega_+ / \omega_- = (a_+ T_+^4) / (a_- T_-^4)$. The fluid velocities on each side in the bubble center frame are given by $v_\pm = \mu(\xi_w, \tilde{v}_\pm)$.

Substituting Eqs. (37) and (38) into Eq. (50), we can solve for \tilde{v}_+ as function of \tilde{v}_- ,

$$\tilde{v}_+ = \frac{1}{1 + \alpha_+} \left[\left(\frac{\tilde{v}_-}{2} + \frac{1}{6\tilde{v}_-} \right) \pm \sqrt{\left(\frac{\tilde{v}_-}{2} + \frac{1}{6\tilde{v}_-} \right)^2 + \alpha_+^2 + \frac{2}{3}\alpha_+ - \frac{1}{3}} \right]. \quad (51)$$

We show the two branches of solutions in Fig. 4. The upper branch corresponds to detonation that the incoming flow is supersonic ($\tilde{v}_+ > c_s$) and is faster than outgoing flow ($\tilde{v}_+ > \tilde{v}_-$). For deflagration $\tilde{v}_+ < c_s$ and $\tilde{v}_+ < \tilde{v}_-$. We can see that there are no deflagration solutions for $\alpha_+ > 1/3$. The process with $\tilde{v}_- = c_s$ is called Jouguet detonation. We then have

$$\tilde{v}_+ = v_J(\alpha_+) = \frac{1 + \sqrt{\alpha_+(2 + 3\alpha_+)}}{\sqrt{3}(1 + \alpha_+)}. \quad (52)$$

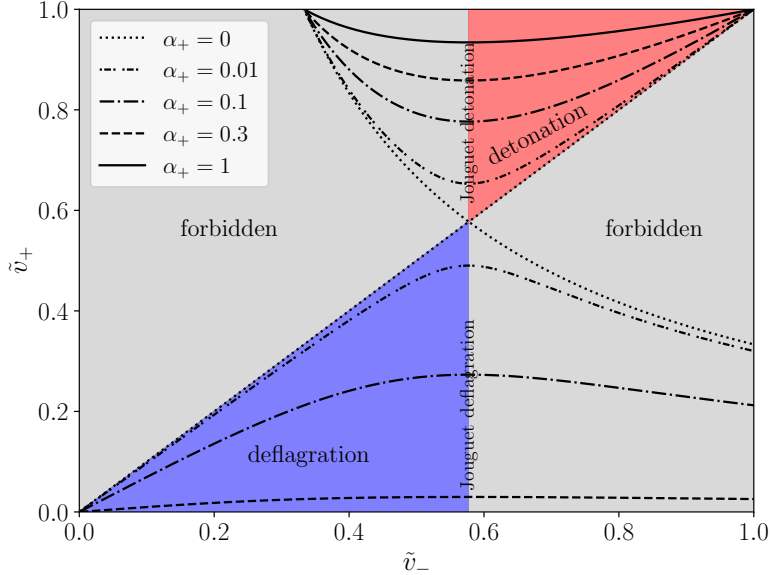


FIG. 4. Velocities in front of and behind the bubble wall. The upper branch and the lower branch correspond to detonation and deflagration respectively. The gray areas are forbidden because they are not physical solutions.

For deflagration mode, in order to satisfy the condition that $v(\xi \rightarrow \infty) = 0$, there should be a shock front at ξ_{sh} in front of the bubble wall. We shall use index 1 for variables behind the shock front and index 2 for variables in front of the shock front. We can get from energy-momentum conservation across the shock front which has a similar form as Eq. (50),

$$\tilde{v}_1 \tilde{v}_2 = \frac{1}{3}, \quad \frac{\tilde{v}_1}{\tilde{v}_2} = \frac{3T_2^4 + T_1^4}{3T_1^4 + T_2^4}. \quad (53)$$

C. spherical approximation

In the spherical case, for detonation we have $v_+ = 0$ in the bubble center frame and $T_+ = T_n$. Then we have $\tilde{v}_+ = \xi_w = v_w$ and $\alpha_+ = \alpha_n$ where $\alpha_n = \epsilon/(a_+ T_n^4)$. The bubble wall is followed by a rarefaction wave which ends at $\xi = c_s$. The rarefaction wave is depicted by continuity equation (46). The boundary condition is

$$v(\xi_w) = v_- = \mu(\xi_w, \tilde{v}_-). \quad (54)$$

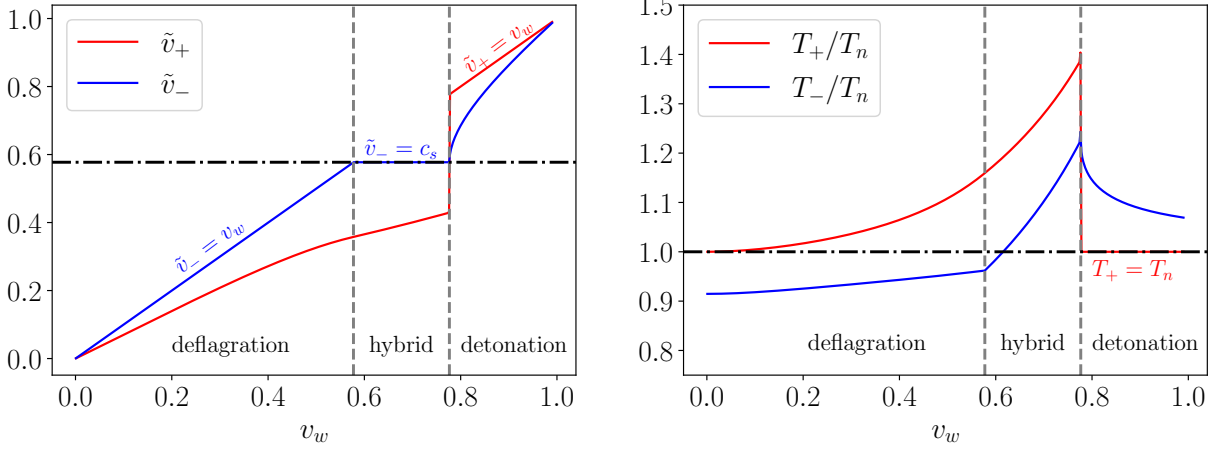


FIG. 5. Left: flow velocity in the bubble wall frame \tilde{v}_+ and \tilde{v}_- as functions of v_w for $\alpha_n = 0.1$ for spherical bubbles. Right: temperature in front of and behind the bubble wall as functions of v_w for $\alpha_n = 0.1$ for spherical bubbles.

with \tilde{v}_- is given by the inverse of Eq. (51). After getting the profile of the velocity, the enthalpy profile is given by Eq. (48) with boundary condition

$$\omega_- = \frac{\gamma_w^2 v_w}{\tilde{\gamma}_-^2 \tilde{v}_-} \omega_n . \quad (55)$$

For deflagration mode, we have $v_- = 0$, $v_2 = 0$ and $\alpha_2 = \alpha_n$. Or equivalently, $\tilde{v}_- = \xi_w = v_w$, $\tilde{v}_2 = \xi_{sh}$ and $\alpha_2 = \alpha_n$. The continuity equation (46) depicts the profile between ξ_w and ξ_{sh} , the the boundary condition is v_+ in front of the bubble wall or v_1 behind the shock front. $v_+ = \mu(\xi_w, \tilde{v}_+)$ with \tilde{v}_+ is given by Eq. (51). However, here $\alpha_+ \neq \alpha_n$ because of the heating effects in front of the bubble wall. In order to solve this, we can use the *shooting method* that we can guess the temperature behind the bubble wall T_- , then from Eq. (50) we get initial values and integrate (46) and (48) up to the point where $\mu(v(\xi), \xi)\xi = 1/3$ to find the position of the shock front. Then adjust T_- until Eq. (53) is satisfied.

For hybrid mode, it has both the shock front and the rarefaction wave. We can use the similar procedure as deflagration, except the boundary condition that $\tilde{v}_- = c_s$.

In Fig. 5, we show the velocity and temperature just in front of and behind the bubble wall and we choose $\alpha_n = 0.1$. For deflagrations we have $\tilde{v}_- = v_w$ and $\tilde{v}_+ < \tilde{v}_-$. For hybrid case we have $\tilde{v}_- = c_s$. For detonations we have $\tilde{v}_+ = v_w$ and $\tilde{v}_- < \tilde{v}_+$. For deflagration

and hybrid modes, there are both heating or cooling in front of and behind the bubble wall. However for detonations we have $T_+ = T_n$ and only heating behind the bubble wall. As we will see in Sec. 8, \tilde{v}_+ and T_+ or \tilde{v}_- and T_- will give the boundary conditions for velocity and temperature profiles across the bubble wall when the wall has nonzero width.

We show the behavior of $\Omega_{\text{DM}}^{(\text{hy})} h^2 / \Omega_{\text{DM}}^{(0)} h^2$ which is the ratio between DM relic abundance in three hydrodynamic mode and DM relic density without heating effects as functions of v_w and D in Fig. 6. In the left panel we show the deflagration case for $v_w < c_s$. The effect of increasing D is mainly increasing α_n . We can see that for low velocity the DM relic density is enhanced which is mainly due to the heating effects from which $T_- < T_n < T_+$ such that $\phi_- < \phi_n$. Then the DM has more ability to pass through the bubble wall. As the velocity increases the effect is weaker. For $v_w \gtrsim 0.1$ we have $\Omega_{\text{DM}}^{(\text{hy})} h^2 / \Omega_{\text{DM}}^{(0)} h^2 < 1$ which is mainly due to the suppression of velocity in front of the bubble wall. This can be seen from $\omega_+ \tilde{\gamma}_+^2 \tilde{v}_+ = \omega_- \tilde{\gamma}_-^2 \tilde{v}_-$ that the variation of velocity is opposite to the temperature. And we can see from Eq. (10) that the variation of the velocity will compensate the variation of the temperature. For detonation case the heating effects influence slightly because the main difference is the vacuum value $\phi_- > \phi_n$ such that $m_\chi^{\text{in}}(T_-) > m_\chi^{\text{in}}(T_n)$. The discontinuity in right panel is due to the jump of temperature and velocity which can be seen in Fig. 5. And we find for $D > 0.7$ there are no solutions for detonations because the heating is strong enough that $T_- > T_c$ ¹. In this case all DM will pass through the bubble wall as their masses behind the wall are zero.

From Eq. (51), in the small limit of bubble wall velocity we have the approximation

$$\tilde{v}_+ \simeq \frac{\tilde{v}_-(1 - 2\alpha_+ - 3\alpha_+^2)}{1 + \alpha_+}. \quad (56)$$

Then from Eq. (49) we have

$$\frac{\omega_-}{\omega_+} = \frac{\tilde{\gamma}_+^2 \tilde{v}_+}{\tilde{\gamma}_-^2 \tilde{v}_-} \simeq \frac{1 - 2\alpha_+ - 3\alpha_+^2}{1 + \alpha_+} \equiv \frac{a_- T_-^4}{a_+ T_+^4}. \quad (57)$$

From Fig. 5 we can see that for $v_w \rightarrow 0$ we have $\alpha_+ \approx \alpha_n$ then

$$\tilde{v}_+ \simeq \frac{v_w(1 - 2\alpha_n - 3\alpha_n^2)}{1 + \alpha_n}, \quad T_- \simeq \left(\frac{1 - 2\alpha_n - 3\alpha_n^2}{1 + \alpha_n} \right)^{\frac{1}{4}} \left(\frac{a_+}{a_-} \right)^{\frac{1}{4}} T_n. \quad (58)$$

For example, in the limit that $v_w = 0.01$, for BP_1 we have $T_- \approx 33$ GeV and then from Eq. (19) we have $\phi(T_-) = 438$ GeV, we can get that $\Omega_{\text{DM}}^{(\text{hy})} h^2 / \Omega_{\text{DM}}^{(0)} h^2 \simeq 65$ which is consistent

¹ This behavior may provide a possibility to achieve super-sonic baryogenesis [28].

with more exact result without using low bubble wall velocity limit. This can be seen in Fig. 6, where we show the $\Omega_{\text{DM}}^{(\text{hy})} h^2 / \Omega_{\text{DM}}^{(0)} h^2$ for different values of D and v_w . We fix $C = 0.04$ and $\lambda = 0.01$. We show the low velocity approximation for $D = 0.4$. It is shown that the low velocity approximation fits well with the exact analytic results.

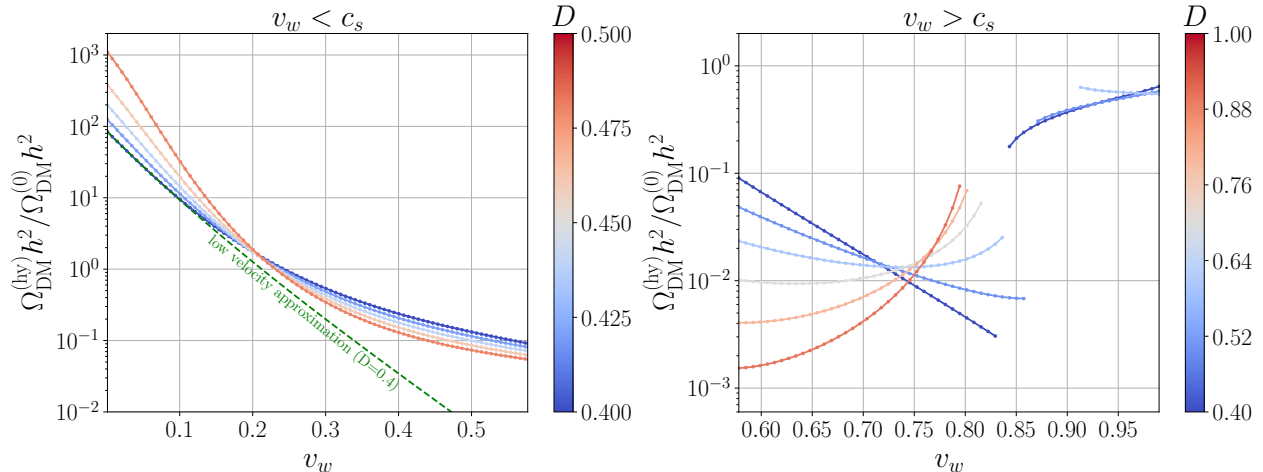


FIG. 6. Ratio of DM relic density $\Omega_{\text{DM}}^{(\text{hy})} h^2 / \Omega_{\text{DM}}^{(0)} h^2$ as function of v_w and D . Left is for $v_w < c_s$ (deflagrations) and right is for $v_w > c_s$ (hybrids and detonations). We fix $C = 0.04$ and $\lambda = 0.01$. And we have fixed $y_\chi = 3$ which gives $\Omega_{\text{DM}}^{(0)} h^2 \simeq 0.12$ when $v_w = 0.01$ for BP_1 .

D. planar approximation

We can get analytic results for planar walls. As $j = 0$ in Eq. (46), we have either $v'(\xi) \equiv 0$ or $\mu(\xi, v) = \pm c_s$. At the bubble wall, the fluid velocity should fulfill $v_\pm < \xi_w$ such that $\mu(\xi, v) = -c_s$ is not physical. Then the physical solutions are either the constants or the rarefaction,

$$v_{\text{rar}}(\xi) = \frac{\xi - c_s}{1 - c_s \xi} \quad (59)$$

The integration in Eq. (48) is simple to do. For $v'(\xi) = 0$ the enthalpy is a constant. For $\mu(\xi, v) = c_s$ we have

$$\frac{\omega}{\omega_0} = \left(\frac{1 - v_0}{1 + v_0} \frac{1 + v}{1 - v} \right)^{2/\sqrt{3}} \quad (60)$$

For detonations, the fluid velocity between $\xi = c_s$ and a certain $\xi_0 \leq \xi_w$ is given by $v(\xi) = v_{rar}(\xi)$. And the fluid velocity between ξ_0 and ξ_w is constant $v \equiv v_-$. From matching condition $v_{rar}(\xi_0) = v_-$ we can determine the position ξ_0 ,

$$\xi_0 = \frac{v_- + c_s}{1 + v_- c_s}. \quad (61)$$

$v_- = \mu(\xi_w, \tilde{v}_-)$ with \tilde{v}_- given by the inverse of Eq. (51) as a function of $\alpha_+ = \alpha_n$ and $\tilde{v}_+ = \xi_w$. Between c_s and ξ_0 , the enthalpy profile is given by Eq. (60) with the boundary condition $\omega_0 = \omega_-$. The ω_- is given by Eq. (55) and is also the constant value between ξ_0 and ξ_w . Inserting Eq. (59) into (60), we have

$$\omega(\xi) = \omega_- \left(\frac{1 - v_-}{1 + v_-} \frac{1 - c_s}{1 + c_s} \frac{1 + \xi}{1 - \xi} \right)^{2/\sqrt{3}}. \quad (62)$$

It is much simpler for deflagration mode. In this case, the fluid velocity is constant $v \equiv v_+ = v_1$ between ξ_w and ξ_{sh} and vanishes outside this region. We also have $\tilde{v}_- = \xi_w$, $\tilde{v}_2 = \xi_{sh}$, $\omega_+ = \omega_1$ and $\alpha_+ = \alpha_1$. Then by using (53), we have

$$3\xi_{sh}^2 = \frac{3\alpha_n + \alpha_1}{\alpha_n + 3\alpha_1}, \quad v_+ = v_1 = \frac{3\xi_{sh}^2 - 1}{2\xi_{sh}} \quad (63)$$

Combine this with Eq. (51) we can get ξ_{sh} as a function of α_n and $\xi_w \equiv v_w$,

$$(3\xi_{sh}^2 - 1)^2 + \xi_{sh}(3\xi_{sh}^2 - 1) \frac{1 - 3\xi_w^2}{\xi_w} = \frac{9}{2} \alpha_n (1 - \xi_{sh}^2)^2 \quad (64)$$

which we can solve numerically.

For hybrid case we get similar equation as Eq. (64) by using the condition $v_+ = v_1$ and $\alpha_+ = \alpha_1$,

$$\left[\xi_{sh}(1 - \sqrt{3}\xi_w) - \frac{3\xi_{sh}^2 - 1}{2}(\xi_w - \sqrt{3}) \right]^2 = \frac{9}{4} \alpha_n (1 - \xi_w^2)(1 - \xi_{sh}^2)^2. \quad (65)$$

In Fig. 7, we show the velocity and enthalpy profile in both spherical and planar cases for $\alpha_n = 0.23$. The solid lines represents the results for spherical bubbles and the dashed lines are for the approximation of planar wall.

V. TEMPERATURE AND VELOCITY PROFILE WITH BUBBLE WALL THICKNESS

Further, we relax the assumption of zero-width bubble wall and consider the wall thickness, which can help to perform more precise results with Boltzmann equations in next

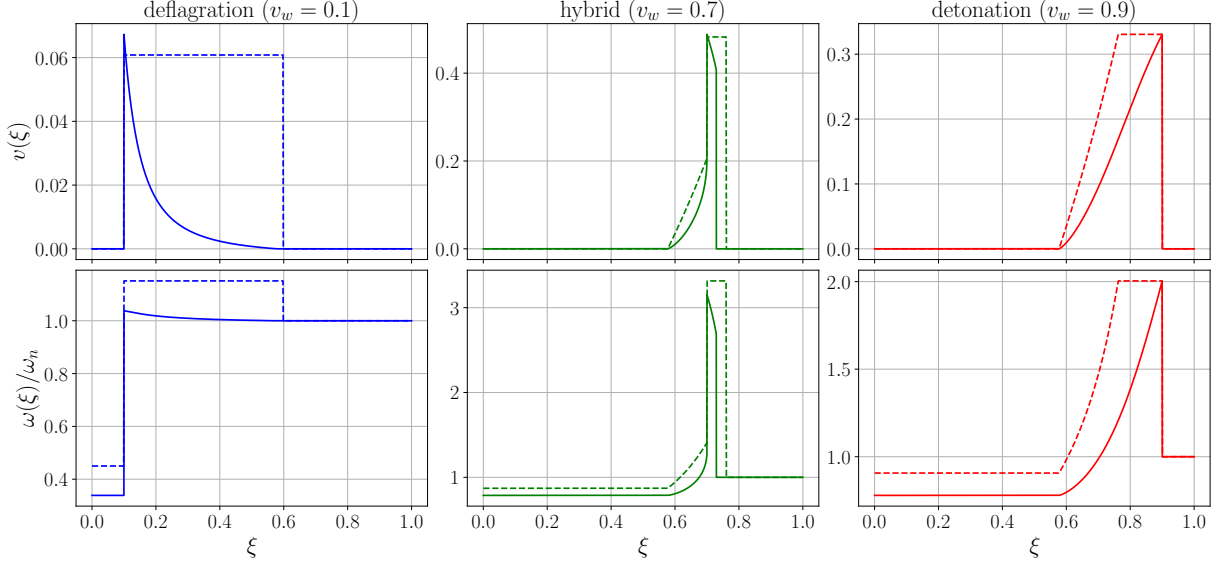


FIG. 7. Velocity and enthalpy profiles of three hydrodynamic modes for $\alpha_n = 0.23$. The solid lines are for spherical bubble and dashed lines are for the approximation of planar wall.

section. As the bubble wall has a finite width, we expect the velocities and temperature of particles have a profile in the wall. Below we neglect the index w of z^w and p_z^w for simplicity. Keep in mind that we work in the bubble wall frame.

To derive the equations that describe the evolution of $T(z)$ and $\tilde{v}_{\text{pl}}(z)$, we can still use the equations of conservation of EMT $\nabla_\mu T^{\mu\nu} = 0$ [29]

$$\begin{aligned} T^{30} &= \omega_{\text{pl}} \tilde{\gamma}_{\text{pl}}^2 \tilde{v}_{\text{pl}} = c_1, \\ T^{33} &= \frac{1}{2} (\partial_z \phi)^2 - V_{\text{eff}}(\phi, T) + \omega_{\text{pl}} \tilde{\gamma}_{\text{pl}}^2 \tilde{v}_{\text{pl}}^2 = c_2, \end{aligned} \quad (66)$$

where c_1 and c_2 are constants that depend on boundary values T_- and \tilde{v}_- (or alternatively on T_+ and \tilde{v}_+), which denote the fluid temperature and velocity at $z \rightarrow \pm\infty$. It is simple to show that, if we parameterize the V_{eff} as

$$V_{\text{eff}} = -p = \epsilon - aT^4/3, \quad (67)$$

this is just the bag model case. However, in reality the a and ϵ is functions of temperature which will give us results beyond bag model [30–32].

In practice, one can directly solve the first line of Eq. (66) for v_{pl} :

$$\tilde{v}_{\text{pl}} = \frac{-\omega_{\text{pl}} + \sqrt{4c_1^2 + \omega_{\text{pl}}^2}}{2c_1}, \quad (68)$$

Substituting \tilde{v}_{pl} into the equation for T^{33} yields

$$\frac{1}{2}(\partial_z \phi)^2 - V_{\text{eff}} - \frac{1}{2}\omega_{\text{pl}} + \frac{1}{2}\sqrt{4c_1^2 + \omega_{\text{pl}}^2} - c_2 = 0, \quad (69)$$

In order to get c_1 and c_2 , we should solve for hydrodynamic equations for bubble wall system just as in last section, in particular, for three cases: detonations, deflagrations and hybrids. As we can see in Fig. 7, we can in many cases just use the planar approximation. Then for three cases, we have:

(a) Detonations: $T_+ = T_n$ and $\tilde{v}_+ = v_w$ which gives us

$$c_1 = \omega_n \gamma_w^2 v_w, \quad c_2 = \omega_n \gamma_w^2 v_w^2 - V_{\text{eff}}(0, T_n). \quad (70)$$

(b) Deflagrations: After getting ξ_{sh} from Eq. (64), we have from (63)

$$\omega_+ = \omega_n \frac{9\xi_{sh}^2}{3(1 - \xi_{sh}^2)}, \quad \tilde{v}_+ = \frac{v_w - v_+}{1 - v_w v_+} \quad \text{where} \quad v_+ = \frac{3\xi_{sh}^2 - 1}{2\xi_{sh}}, \quad (71)$$

then

$$c_1 = \omega_+ \tilde{\gamma}_+^2 \tilde{v}_+, \quad c_2 = \omega_+ \tilde{\gamma}_+^2 \tilde{v}_+^2 - V_{\text{eff}}(0, T_+). \quad (72)$$

(c) Hybrids: After solving ξ_{sh} from Eq. (65), we have the same form of c_1 and c_2 as deflagrations.

After getting c_1 and c_2 , we can solve Eqs. (68) and (69) to get the profiles of velocity $\tilde{v}_{\text{pl}}(z)$ and temperature $T(z)$ around the bubble wall.

In addition to Eqs. (68) and (69), we have another equation, i.e. the EOM of the background scalar field,

$$\partial^2 \phi + \frac{\partial V_{\text{eff}}(\phi, T)}{\partial \phi} = 0. \quad (73)$$

A simple solution of this equation is *tanh* ansatz,

$$\phi(z) = \frac{\phi(T_-)}{2} \left(1 + \tanh \frac{2z}{L_w} \right). \quad (74)$$

We choose the wall width $L_w = 5/T_n$. We show the results of $T(z)$ and $\tilde{v}_{\text{pl}}(z)$ in Fig. 8 where we choose relatively low velocity $v_w = 0.01$ and relatively high velocity $v_w = 0.9$, respectively. The left figure represents the deflagration mode where the temperature inside the bubble wall is lower than T_n . We can also see that $\tilde{v}_- = v_w$ which fulfills the boundary condition for deflagration. In contrast, the right figure depicts the detonation mode where the temperature in front of the bubble wall $T_+ = T_n$ and temperature inside bubble wall is higher than T_n . For detonation we also have $\tilde{v}_+ = v_w$.

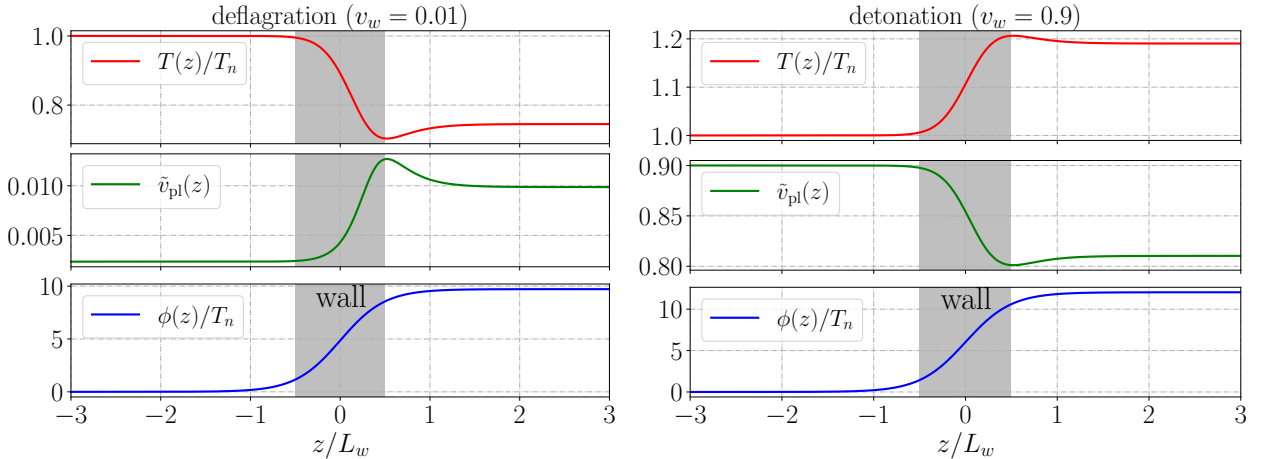


FIG. 8. Velocity and temperature profiles of DM across the bubble wall for deflagration ($v_w = 0.01$) and detonation ($v_w = 0.9$). The hydrodynamic effects and bubble width are considered.

VI. NUMERICAL RESULTS OF THE HYDRODYNAMIC EFFECTS ON BOLTZMANN EQUATION WITH BUBBLE WALL THICKNESS

To obtain more precise results of the hydrodynamic effects on the DM density, we perform numerical calculations with Boltzmann equations and bubble wall thickness.

A. Boltzmann equation

The Boltzmann equation describe the phase space evolution of the particles,

$$\mathbf{L}[f_\chi] = \mathbf{C}[f_\chi] . \quad (75)$$

Here, \mathbf{L} is the Liouville operator and \mathbf{C} is a collision term, which accounts for the particle interactions.

We introduce fluid ansatz, in the wall frame the distribution function of DM is parameterized as

$$f_\chi = \mathcal{A}(z, p_z) f_{\chi,+}^{\text{eq}} = \mathcal{A}(z, p_z) \exp\left(-\frac{\tilde{\gamma}_+(E - \tilde{v}_+ p_z)}{T_+}\right) , \quad (76)$$

where $f_{\chi,+}^{\text{eq}}$ is the equilibrium distribution function in front of the bubble wall. $E =$

$\sqrt{p_x^2 + p_y^2 + p_z^2 + m_\chi(z)^2}$ with

$$m_\chi(z) \equiv \frac{m_\chi^{\text{in}}(\phi_-)}{2} \left(1 + \tanh \frac{2z}{L_w} \right), \quad (77)$$

where $m_\chi^{\text{in}}(\phi_-) = y_\chi \phi_-$ is the mass of DM deep inside the bubble.

The Liouville operator is the total time derivative of the phase space distribution function $f = f(t, \mathbf{x}(t), \mathbf{p}(t))$. In a steady state and neglect the x, y direction, using energy-conservation $p_z^2 + m_\chi(z)^2 = \text{const}$ in the wall frame, we then have

$$\mathbf{L}[f_\chi] = \frac{p_z}{E} \frac{\partial f_\chi}{\partial z} - \frac{m_\chi}{E} \frac{\partial m_\chi}{\partial z} \frac{\partial f_\chi}{\partial p_z}. \quad (78)$$

We now integrate over the transverse momentum components p_x and p_y and multiply by the number of spin states, $g_\chi = 2$, giving

$$g_\chi \int \frac{dp_x dp_y}{(2\pi)^2} \mathbf{L}[f_\chi] = g_\chi \int \frac{dp_x dp_y}{(2\pi)^2} \frac{p_z}{E} \frac{\partial f_\chi}{\partial z} - g_\chi \left(\frac{\partial m_\chi}{\partial z} \right) \int \frac{dp_x dp_y}{(2\pi)^2} \frac{m_\chi}{E} \frac{\partial f_\chi}{\partial p_z}. \quad (79)$$

Using the Maxwell-Boltzmann approximation for f_χ then gives

$$\begin{aligned} g_\chi \int \frac{dp_x dp_y}{(2\pi)^2} \mathbf{L}[f_\chi] &\approx g_\chi \left(\frac{\partial}{\partial z} \mathcal{A}(z, p_z) \right) \int \frac{dp_x dp_y}{(2\pi)^2} \frac{p_z}{\sqrt{m_\chi^2 + p_x^2 + p_y^2 + p_z^2}} e^{-E_+^P/T_+} \\ &+ g_\chi \mathcal{A}(z, p_z) \int \frac{dp_x dp_y}{(2\pi)^2} \frac{p_z}{\sqrt{m_\chi^2 + p_x^2 + p_y^2 + p_z^2}} \left(\frac{\partial}{\partial z} e^{-E_+^P/T_+} \right) \\ &- g_\chi \left(\frac{\partial m_\chi}{\partial z} \right) \left(\frac{\partial}{\partial p_z} \mathcal{A}(z, p_z) \right) \int \frac{dp_x dp_y}{(2\pi)^2} \frac{m_\chi}{\sqrt{m_\chi^2 + p_x^2 + p_y^2 + p_z^2}} e^{-E_+^P/T_+} \\ &- g_\chi \left(\frac{\partial m_\chi}{\partial z} \right) \mathcal{A}(z, p_z) \int \frac{dp_x dp_y}{(2\pi)^2} \frac{m_\chi}{\sqrt{m_\chi^2 + p_x^2 + p_y^2 + p_z^2}} \left(\frac{\partial}{\partial p_z} e^{-E_+^P/T_+} \right), \end{aligned} \quad (80)$$

where

$$E_+^P \equiv E_+^P(z, p_z) = \tilde{\gamma}_+(z)(E - \tilde{v}_+ p_z), \quad (81)$$

After the integration the Liouville term becomes

$$\begin{aligned} g_\chi \int \frac{dp_x dp_y}{(2\pi)^2} \mathbf{L}[f_\chi] &\approx \\ &\left[\left(\frac{p_z}{m_\chi} \frac{\partial}{\partial z} - \left(\frac{\partial m_\chi}{\partial z} \right) \frac{\partial}{\partial p_z} - \left(\frac{\partial m_\chi}{\partial z} \right) \frac{\tilde{\gamma}_+ \tilde{v}_+}{T_+} \right) \mathcal{A}(z, p_z) \right] \frac{g_\chi m_\chi T_+}{2\pi \tilde{\gamma}_+} e^{\tilde{\gamma}_+(\tilde{v}_+ p_z - \sqrt{m_\chi^2 + p_z^2})/T_+}. \end{aligned} \quad (82)$$

B. Collision term

We evaluate the collision term $\mathbf{C}[f_\chi]$ in the local plasma frame of DM and turn back to wall frame at last. We consider the process of inverse decay $\chi(p^\mathcal{P}) + \bar{\chi}(q^\mathcal{P}) \rightarrow \phi(k^\mathcal{P})$ and annihilation $\chi(p^\mathcal{P}) + \bar{\chi}(q^\mathcal{P}) \rightarrow \phi(k^\mathcal{P}) + \phi(l^\mathcal{P})$ in our case. The collision terms for the other processes, $\chi\phi \rightarrow \chi\phi$, $\chi\chi \rightarrow \chi\chi$ and $\chi\bar{\chi} \rightarrow \chi\bar{\chi}$, has similar expressions. For annihilation, integrating over p_x and p_y and multiplying by the number of spin states, $g_\chi = 2$, the collision term is

$$g_\chi \int \frac{dp_x dp_y}{(2\pi)^2} \mathbf{C}[f_\chi] = - \sum_{\text{spins}} \int \frac{dp_x dp_y}{(2\pi)^2} d\Pi_{q^\mathcal{P}} d\Pi_{k^\mathcal{P}} d\Pi_{l^\mathcal{P}} \frac{(2\pi)^4}{2E_p^\mathcal{P}} \delta^{(4)}(p^\mathcal{P} + q^\mathcal{P} - k^\mathcal{P} - l^\mathcal{P}) |\mathcal{M}|^2 \quad (83)$$

$$\cdot [f_{\chi_p} f_{\bar{\chi}_q} (1 \pm f_{\phi_k}) (1 \pm f_{\phi_l}) - f_{\phi_k} f_{\phi_l} (1 \pm f_{\chi_p}) (1 \pm f_{\bar{\chi}_q})] ,$$

where \mathcal{M} is the scattering matrix element, and we have used the notation $E_p^\mathcal{P} = [(\mathbf{p}^\mathcal{P})^2 + m_\chi^2]^2$, $d\Pi_{q^\mathcal{P}} \equiv d^3q^\mathcal{P} / [2E_q^\mathcal{P}(2\pi)^3]$, and $f_{\chi_p} \equiv f_\chi(t^\mathcal{P}, \mathbf{x}^\mathcal{P}, \mathbf{p}^\mathcal{P})$, with $\chi_p \equiv \chi(p)$.

We neglect Pauli blocking and Bose enhancement for all species by setting $1 \pm f \approx 1$, and we assume that all species except for the initial DM particle $\chi(p)$ are in equilibrium. In the local frame of plasma of DM the light particles ϕ should obey the equilibrium distribution

$$f_\phi^{\text{eq}} = \exp\left(-\frac{\tilde{\gamma}'_{\text{pl}}(z)(E_\phi - \tilde{v}'_{\text{pl}}(z)p_{z\phi})}{T(z)}\right) , \quad (84)$$

along the path into bubble, where

$$\tilde{v}'_{\text{pl}}(z) = \frac{\tilde{v}_{\text{pl}}(z) - \tilde{v}_+}{1 - \tilde{v}_{\text{pl}}(z)\tilde{v}_+} \quad (85)$$

is the relativistic velocity between ϕ and DM.

Since detailed balance holds for each momentum mode independently, $f_{\phi_k}^{\text{eq}} f_{\phi_l}^{\text{eq}} = f_{\chi_p}^{\text{eq}} f_{\bar{\chi}_q}^{\text{eq}}$.

$$g_\chi \int \frac{dp_x dp_y}{(2\pi)^2} \mathbf{C}[f_\chi] = -g_\chi \int \frac{dp_x dp_y}{(2\pi)^2} d\Pi_{q^\mathcal{P}} d\Pi_{k^\mathcal{P}} d\Pi_{l^\mathcal{P}} \frac{(2\pi)^4}{2E_p^\mathcal{P}} \delta^{(4)}(p^\mathcal{P} + q^\mathcal{P} - k^\mathcal{P} - l^\mathcal{P}) |\mathcal{M}|^2$$

$$\times [f_{\chi_p}^{\text{eq}} f_{\bar{\chi}_q, +}^{\text{eq}} - f_{\chi_p}^{\text{eq}} f_{\bar{\chi}_q}^{\text{eq}}] . \quad (86)$$

Here we approximate $f_{\bar{\chi}_q} \simeq f_{\bar{\chi}_q, +}^{\text{eq}}$. We will see later the \mathcal{A} is $\mathcal{O}(1)$ except for some finite region, so this approximation doesn't influence the results dramatically.

We can now integrate over k and l to obtain

$$\begin{aligned}
g_\chi \int \frac{dp_x dp_y}{(2\pi)^2} \mathbf{C} [f_\chi] &= -g_\chi g_{\bar{\chi}} \int \frac{dp_x dp_y}{(2\pi)^2 2E_p^{\mathcal{P}}} d\Pi_{q^{\mathcal{P}}} 4F \sigma_{\chi\bar{\chi} \rightarrow \phi\phi} \left[f_{\chi_p} f_{\bar{\chi}_{q,+}}^{\text{eq}} - f_{\chi_p}^{\text{eq}} f_{\bar{\chi}_q} \right] \\
&= -g_\chi g_{\bar{\chi}} \int \frac{dp_x dp_y}{(2\pi)^2 2E_p^{\mathcal{P}}} d\Pi_{q^{\mathcal{P}}} 4F \sigma_{\chi\bar{\chi} \rightarrow \phi\phi} \left[\mathcal{A} f_{\chi_p,+}^{\text{eq}} + f_{\bar{\chi}_{q,+}}^{\text{eq}} - f_{\chi_p}^{\text{eq}} f_{\bar{\chi}_q}^{\text{eq}} \right] \quad (87) \\
&= \Gamma_{\mathcal{P}}(z, p_z) \mathcal{A}(z, p_z) - \Gamma_{\mathcal{I}}(z, p_z) ,
\end{aligned}$$

where the kinematic factor,

$$F \equiv E_p^{\mathcal{P}} E_q^{\mathcal{P}} |v_\chi - v_{\bar{\chi}}| = \frac{1}{2} \sqrt{(s - 2m_\chi^2)^2 - 4m_\chi^4} , \quad (88)$$

and here we define the collision rate for $\chi\bar{\chi} \rightarrow \phi\phi$

$$\Gamma_{\mathcal{P}}(z, p_z) = -g_\chi g_{\bar{\chi}} \int \frac{dp_x dp_y}{(2\pi)^2 2E_p^{\mathcal{P}}} d\Pi_{q^{\mathcal{P}}} 4F \sigma_{\chi\bar{\chi} \rightarrow \phi\phi} f_{\chi_p,+}^{\text{eq}} + f_{\bar{\chi}_{q,+}}^{\text{eq}} , \quad (89)$$

and collision rate for their inverse process

$$\Gamma_{\mathcal{I}}(z, p_z) = -g_\chi g_{\bar{\chi}} \int \frac{dp_x dp_y}{(2\pi)^2 2E_p^{\mathcal{P}}} d\Pi_{q^{\mathcal{P}}} 4F \sigma_{\chi\bar{\chi} \rightarrow \phi\phi} f_{\chi_p}^{\text{eq}} f_{\bar{\chi}_q}^{\text{eq}} . \quad (90)$$

To boost back into bubble wall frame, in Eq. (89) we should replace $E_p^{\mathcal{P}}$ with $\tilde{\gamma}_+(E - \tilde{v}_+ p_z)$ and in Eq. (90) with $\tilde{\gamma}_{\text{pl}}(z)(E - \tilde{v}_{\text{pl}}(z)p_z)$.

In the case without heating, we have $\tilde{v}_+ = v_w$ and $T_+ = T_n$, then we have

$$g_\chi \int \frac{dp_x dp_y}{(2\pi)^2} \mathbf{C} [f_\chi] = \Gamma_n(z, p_z) (\mathcal{A}(z, p_z) - 1) \quad (91)$$

with $\Gamma_{\mathcal{P}} = \Gamma_{\mathcal{I}} = \Gamma_n$. This is the original form of Ref. [2].

Outside the bubble, where $m_\chi \approx 0$, the annihilation cross section is

$$\sigma(\chi\bar{\chi} \rightarrow \phi\phi) = \frac{y_\chi^4}{32\pi s} \left[2 \log(s/m_\phi^2) - 3 \right] + \mathcal{O}(m_\phi^2/s) . \quad (92)$$

We show in Fig. 9 the collision rate $\Gamma(z, p_z)$ for $y_\chi = 1$ and $p_z^{\text{in}} = 600$ GeV where p_z^{in} is the incident z -momentum. As we can see, due to the hydrodynamic effects, the collision rates are different for each case. The detonation case has the same temperature in front of the bubble wall such that the same collision rate. However, because of the heating effects behind the bubble wall, T_- is larger although the VEV is larger. This induces larger collision rate for $\Gamma_{\mathcal{I}}$. And because of $T_+ = T_n < T_-$ and $\phi_- > \phi_n$, we also have that $\Gamma_{\mathcal{P}} < \Gamma_n < \Gamma_{\mathcal{I}}$. For deflagration of $v_w = 0.01$, as the plasma in front of the bubble wall is heated, the collision rate is slightly enhanced. Due to that $T_- < T_n < T_+$ and $\phi_- < \phi_n$, we have $\Gamma_{\mathcal{I}} < \Gamma_n < \Gamma_{\mathcal{P}}$.

For decay process, we have

$$\begin{aligned}
g_\chi \int \frac{dp_x dp_y}{(2\pi)^2} \mathbf{C}[f_\chi] &= -g_\chi \int \frac{dp_x dp_y}{(2\pi)^2} d\Pi_{q^\mathcal{P}} d\Pi_{k^\mathcal{P}} \frac{(2\pi)^4}{2E_p^\mathcal{P}} \delta^{(4)}(p^\mathcal{P} + q^\mathcal{P} - k^\mathcal{P}) |\mathcal{M}|^2 [f_{\chi_p} f_{\bar{\chi}_q, +}^{\text{eq}} - f_{\phi_k}^{\text{eq}}] \\
&= -g_\chi \int \frac{dp_x dp_y}{(2\pi)^2} d\Pi_{q^\mathcal{P}} d\Pi_{k^\mathcal{P}} \frac{(2\pi)^4}{2E_p^\mathcal{P}} \delta^{(4)}(p^\mathcal{P} + q^\mathcal{P} - k^\mathcal{P}) |\mathcal{M}|^2 [\mathcal{A} f_{\chi_p, +} f_{\bar{\chi}_q, +}^{\text{eq}} - f_{\bar{\chi}_p}^{\text{eq}} f_{\bar{\chi}_q}^{\text{eq}}] \\
&= \Gamma_{\text{P}}(z, p_z) \mathcal{A}(z, p_z) - \Gamma_{\text{I}}(z, p_z) , \tag{93}
\end{aligned}$$

with

$$\Gamma_{\text{I(P)}}(z, p_z) = - \int dp_x dp_y dq^\mathcal{P} \frac{g_\chi g_{\bar{\chi}} m_\phi^2 q^\mathcal{P}}{128\pi^4 E_p^\mathcal{P} E_q^\mathcal{P} p^\mathcal{P}} f_{\bar{\chi}_p(+)}^{\text{eq}} f_{\bar{\chi}_q(+)}^{\text{eq}} , \tag{94}$$

where we have used for inverse decay $|\mathcal{M}|^2 = 4y_\chi^2(p \cdot q)$ and then integrate the phase space.

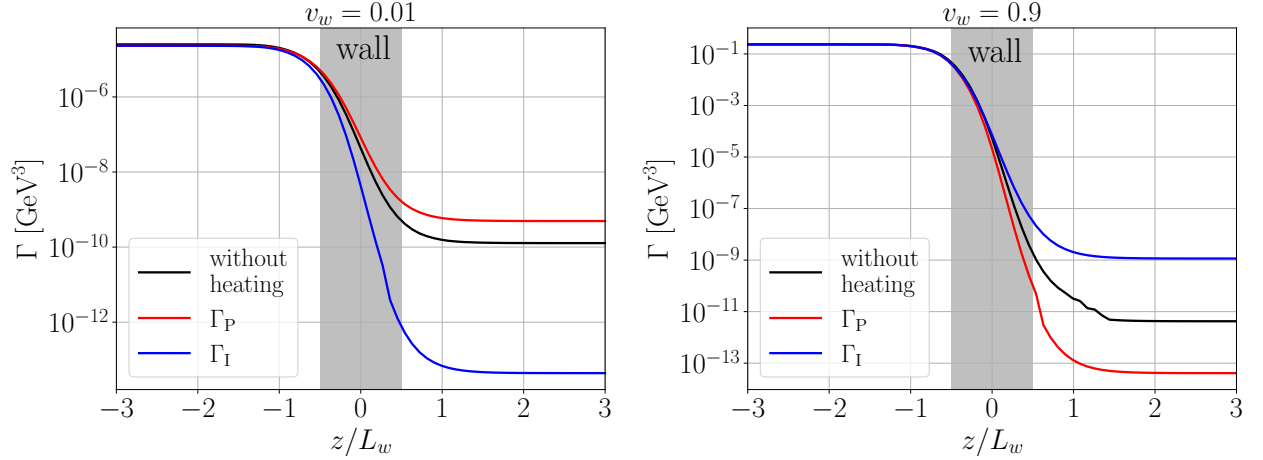


FIG. 9. Collision rates for $p_z^{\text{in}} = 600$ GeV. Red and blue lines are collision rates considering heating effects and black lines are collision rates without heating effects. Left panel is for $v_w = 0.01$ and right panel is for $v_w = 0.9$.

C. Numerical results

1. Solutions to Boltzmann equations

Due to energy and momentum conservation, along the paths on which both the transverse momentum p_\perp and the quantity $p_z^2 + m^2(z)$ are constant, the differential operator simply

reduces to a total derivative with respect to z :

$$\frac{p_z}{m_\chi} \frac{\partial}{\partial z} - \left(\frac{\partial m_\chi}{\partial z} \right) \frac{\partial}{\partial p_z} \rightarrow \frac{p_z}{m_\chi} \frac{d}{dz}, \quad (95)$$

which is called *the method of characteristics*.

Then the Boltzmann equations can be transformed into the form of

$$\frac{d\mathcal{A}}{dz} = c(\mathcal{A}, p_z, z) . \quad (96)$$

The explicit form of right-handed term can be extracted from Eqs. (82) and (87).

In order to solve for this differential equation we have to impose the boundary conditions. As the particles far in front of the bubble wall should be in thermal equilibrium, we can set $\mathcal{A}(z \ll -L_w, p_z > 0) = 1$. This uses the thermal-equilibrium condition which we discuss in Appendix B. We also assume a identical parallel wall at $z \gg L_w$. We can compute the solutions along the curves starting at $(z \ll -L_w, p_z > m_\chi^{\text{in}})$ to find the values deep inside the bubble, at $(z \gg L_w, p_z > 0)$. Then for particles which originate inside the bubble wall we set

$$\mathcal{A}(z \gg L_w, p_z) = \mathcal{A}(z \gg L_w, -p_z) . \quad (97)$$

This assumes that the flow form inside to outside comes from the other side of bubble wall.

After getting $\mathcal{A}(z, p_z)$, we can integrate and get the DM relic number density

$$n_\chi^{\text{in}} = \frac{T_+}{\gamma_w \tilde{\gamma}_+} \int_0^\infty \frac{dp_z}{(2\pi)^2} \mathcal{A}(z \gg L_w, p_z) \exp \left[\tilde{\gamma}_+ \left(\tilde{v}_+ p_z - \sqrt{p_z^2 + (m_\chi^{\text{in}})^2} \right) / T_+ \right] \left(\sqrt{p_z^2 + (m_\chi^{\text{in}})^2} + \frac{T_+}{\tilde{\gamma}_+} \right) , \quad (98)$$

where the extra $1/\gamma_w$ account for the boost from bubble wall frame into bubble center frame.

We show the phase space enhancement factor \mathcal{A} in Fig. 10. We can see that for $v_w = 0.01$ it is dramatically different for cases with or without heating. Due to the heating effects in deflagration mode, the phase space enhancement factor is smaller because of the smaller velocity in front of the wall and smaller m_χ^{in} behind the bubble wall. Smaller m_χ^{in} causes smaller perturbations for DM. For detonations the velocity is same for both cases but m_χ^{in} for detonations is slightly larger due to the heating effect, \mathcal{A} is slightly larger.

One may worry about the too large \mathcal{A} of our results. However, the \mathcal{A} evaluate the non-equilibrium part of distribution function of DM. When DM mass is very large compared with temperature, it is almost fully decouple with SM bath and we hope the non-equilibrium part should be large. This can be seen from the extreme case that the DM decouple with thermal

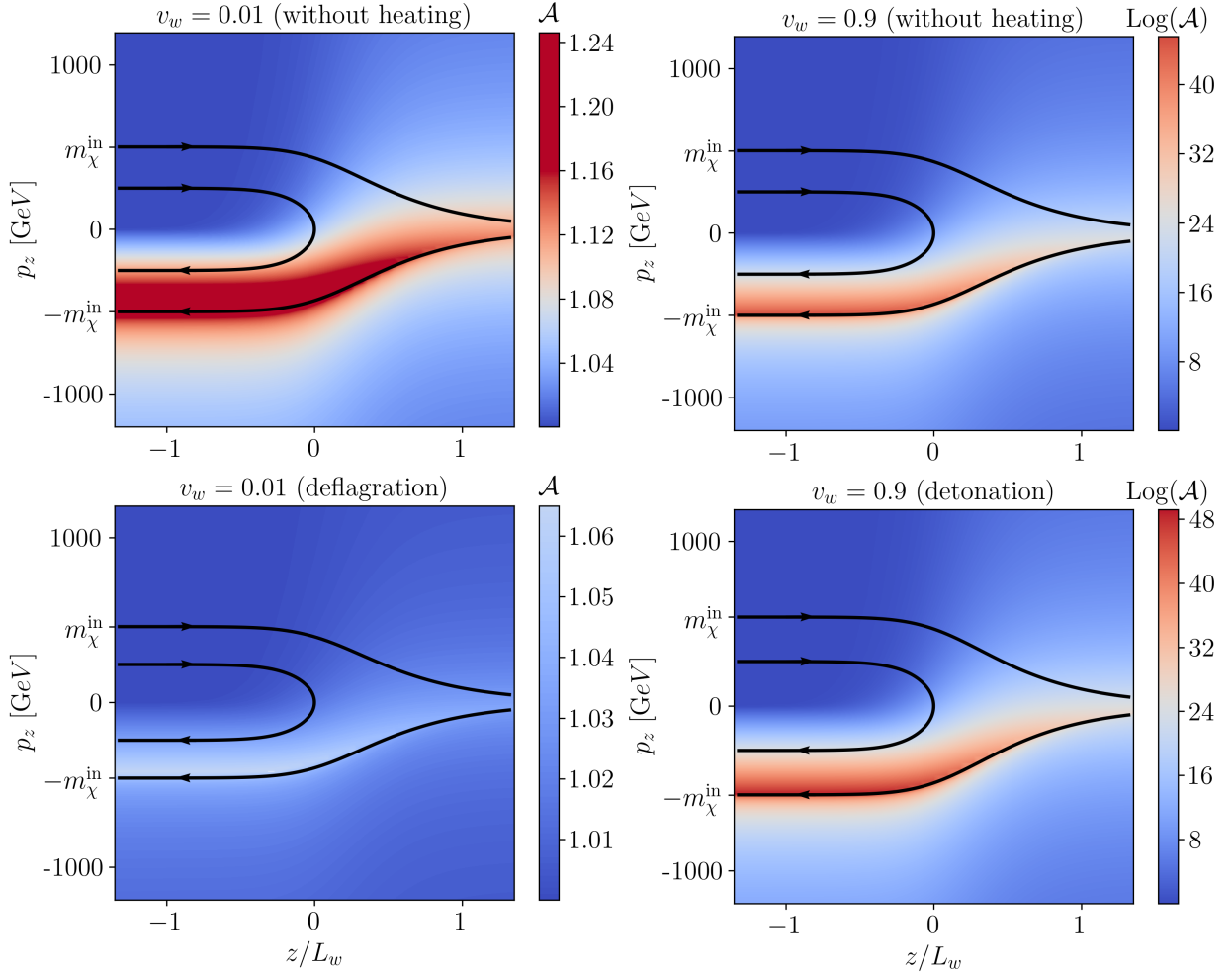


FIG. 10. Evolution of $\mathcal{A}(z, p_z)$ where we choose $y_\chi = 1$. Left panel is for low velocity $v_w = 0.01$ and right panel is for high velocity $v_w = 0.9$.

bath immediately when DM hit the bubble wall, in other words the DM is in purely non-equilibrium state. Then we can ignore the collision term in Boltzmann equation. Thus we have

$$\frac{d}{dz}(\mathcal{A}f_\chi^{\text{eq}}) = 0 \quad (99)$$

along the flow path of DM. This gives us

$$\mathcal{A}(z \gg L_w, p_z) \exp\left(-\frac{\tilde{\gamma}_+(E - \tilde{v}_+ p_z)}{T_+}\right) = \mathcal{A}(z \ll -L_w, p_z^{\text{in}}) \exp\left(-\frac{\tilde{\gamma}_+(E - \tilde{v}_+ p_z^{\text{in}})}{T_+}\right) \quad (100)$$

Because we have $\mathcal{A}(z \ll -L_w, p_z^{\text{in}}) = 1$ and energy-conservation $p_z^2 + m_\chi^2 = \text{const.}$ we can

get $p_z^{\text{in}} = p_z^2 + (m_\chi^{\text{in}})^2$, which gives us

$$\mathcal{A}(z \gg L_w, p_z) = \exp\left(\frac{\tilde{\gamma}_+ \tilde{v}_+ (\sqrt{p_z^2 + (m_\chi^{\text{in}})^2} - p_z)}{T_+}\right). \quad (101)$$

This can obviously be very large. Generally, the collision with thermal bath help DM to return to thermal equilibrium, so we expect a smaller \mathcal{A} when we include the collision term.

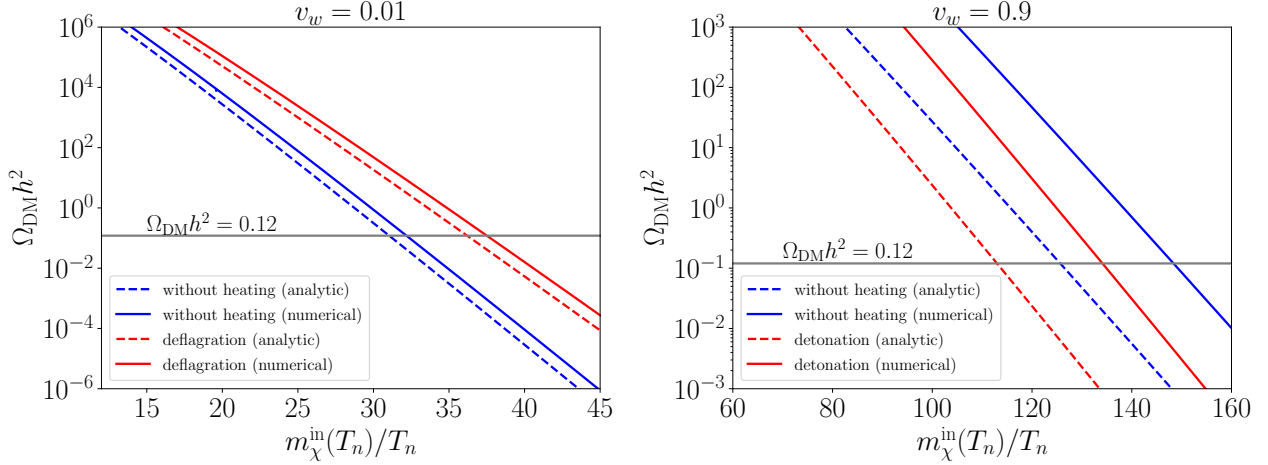


FIG. 11. $\Omega_{\text{DM}} h^2$ as functions of $m_\chi^{\text{in}}(T_n)/T_n$ with $m_\chi^{\text{in}}(T_n) \equiv y_\chi \phi_n$ with and without hydrodynamic heating effects.

From Fig. 11 we show the DM relic density for BP_1 and we choose $v_w = 0.01$. We find for analytic results, the DM relic density for deflagration mode is almost 65 times the one without heating. For numerical results the DM relic density for case for deflagration is almost 70 times the one without heating. For detonations we have $\Omega_{\text{DM}}^{(\text{hy})} h^2 / \Omega_{\text{DM}}^{(0)} h^2 = 1/19$ in analytic method and $\Omega_{\text{DM}}^{(\text{hy})} h^2 / \Omega_{\text{DM}}^{(0)} h^2 = 1/27$ in numerical method. This heating effects are weaker than deflagration because of that for detonation the only difference is the temperature behind the bubble wall and so the DM field-dependent mass m_χ^{in} .

2. Results for benchmark points

We show the results for four benchmark points in Tab. II and Tab. III for $v_w = 0.01$ and $v_w = 0.9$, respectively. As we can see in Tab. II, for $v_w = 0.01$ the DM relic density is

	analytic		numerical	
	$m_\chi^{\text{in}}(T_n)/T_n$	$\Omega_{\text{DM}}^{(\text{hy})}h^2/\Omega_{\text{DM}}^{(0)}h^2$	$m_\chi^{\text{in}}(T_n)/T_n$	$\Omega_{\text{DM}}^{(\text{hy})}h^2/\Omega_{\text{DM}}^{(0)}h^2$
BP_1	31	66	32	71
BP_2	31.1	7.9	32.2	8.1
BP_3	30.8	778.8	31.9	858.5
BP_4	*	*	*	*

TABLE II. Results for the four benchmark points for $v_w = 0.01$. The $m_\chi^{\text{in}}(T_n)/T_n$ is set by $\Omega_{\text{DM}}^{(0)}h^2 = 0.12$. For BP_4 there is no deflagration mode because of the large phase-transition strength α_n .

	analytic		numerical	
	$m_\chi^{\text{in}}(T_n)/T_n$	$\Omega_{\text{DM}}^{(\text{hy})}h^2/\Omega_{\text{DM}}^{(0)}h^2$	$m_\chi^{\text{in}}(T_n)/T_n$	$\Omega_{\text{DM}}^{(\text{hy})}h^2/\Omega_{\text{DM}}^{(0)}h^2$
BP_1	125.3	1/19	147.8	1/27
BP_2	125.9	1/7	148.7	1/9
BP_3	124.6	1/10	147.3	1/12
BP_4	123.8	$1/(1.2 \times 10^{13})$	146.5	$1/(2.2 \times 10^{15})$

TABLE III. Results for the four benchmark points for $v_w = 0.9$. $BP_{1,2,3}$ are detonation cases and BP_4 is the hybrid case.

generally enhanced due to the heating effects. And the enhancement is bigger as the phase-transition strength α_n is larger. This is because that there is larger difference of temperature and velocity between the in front of and behind the bubble wall. For BP_4 with $v_w = 0.01$, there is no deflagration mode for $\alpha_+ > 1/3$.

And in Tab. III, we find for detonation mode the DM relic density is generally lower than which without heating. The difference generally have one or two order of magnitude. The effects are slighter as the phase-transition strength is smaller. Note that for BP_4 the case is actually hybrid mode, such that the effects are extremely significant. This can be seen from Eq. (52) that for BP_4 we have $v_J(\alpha_n) \simeq 0.92$. The effects for hybrid case are large because for hybrid mode there are both large effects in front of and behind the bubble wall. However, for detonation we have only heating effects behind the bubble wall which influence the vacuum value of the field.

VII. PHASE TRANSITION GRAVITATIONAL WAVE SIGNALS OF THE FILTERED DARK MATTER

Naturally, this filtered DM could be detected by phase transition GW from bubble collision [33–35], turbulence [35] and sound wave [36] during a SFOPT. We just show the phase transition GW spectra for BP_2 , BP_3 , and BP_4 with $v_w = 0.9$ in Fig. 12. The colored regions represent the sensitivity curves for LISA [37] and TianQin [38] with the signal-to-noise ratio (SNR) about 5 for 10^8 s observation time, respectively. The GW spectra are sensitive to bubble wall velocity. For example, for $v_w = 0.01$, the GW spectrum is much more weaker. The corresponding SNR will be lower than 5. From Fig. 12, we could see that the future GW detectors LISA, TianQin [39] could detect this new DM mechanism with SNR larger than 5. Taiji [40], BBO [41], DECIGO [42], Ultimate-DECIGO [43] could also detect this new DM mechanism by GW signals.

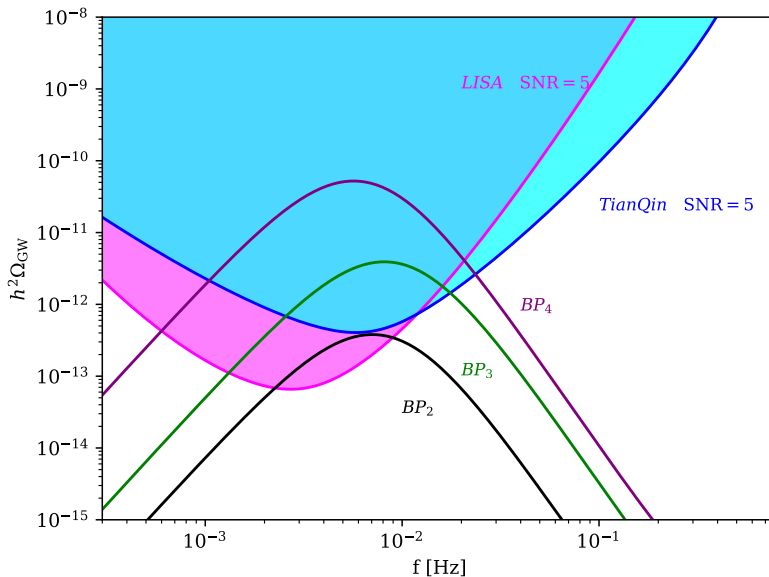


FIG. 12. Phase transition GW spectra for BP_2 , BP_3 , and BP_4 . The colored regions represent the sensitivity curves for LISA and TianQin with SNR= 5 for 10^8 s observation time, respectively

VIII. CONCLUSION

We have find that the hydrodynamic effects play essential roles in the filtered DM mechanism and can significantly change the DM relic density. On one hand, to produce efficient filtered effects, the wash out parameter ϕ/T is usually very large, which usually corresponds to large phase transition strength α . And for large α , the hydrodynamic effects are significant since in this case, the temperature and velocity differences in front of and behind the bubble wall are significant. On the other hand, the bubble wall velocity and the hydrodynamic mode are also essential to the final relic DM density. For deflagration mode with low bubble wall velocity, the hydrodynamic effects significantly enhance the relic density. For detonation mode, the relic density is obviously reduced. For hybrid mode, the hydrodynamic correction is extremely large. Our study could be applied in various concrete filtered DM models.

ACKNOWLEDGMENTS

The authors thank Chang Sub Shin for helpful correspondence. We acknowledge Zheng-Cheng Liang to provide the updated sensitivity curve. This work is supported by the National Natural Science Foundation of China (NNSFC) under Grant No. 12205387.

Appendix A: Phase transition parameters

This is the results from Ref.[17]

$$\alpha = \frac{15(\sqrt{9-4\delta}+3)(-4\delta+3\sqrt{9-4\delta}+9)C^2(D\lambda-\delta C^2)}{2^3\pi^2\sqrt{9-4\delta}g_*\lambda^3}, \quad (\text{A1})$$

and

$$\frac{\beta}{H} = \frac{192\pi\sqrt{\delta}[-\beta_1(\delta+6)+\beta_2\delta(\delta-10)+\beta_3\delta^2(3\delta-14)](D\lambda-\delta C^2)}{243(\delta-2)^3C\lambda^{3/2}}. \quad (\text{A2})$$

with β_1 , β_2 and β_3 given in Eq. (21).

In Fig. 13 we show the bounce action $S_3(T)/T$ as function of temperature. We can see that the the CosmoTransitions gives the same results as the semi-analytic calculation.

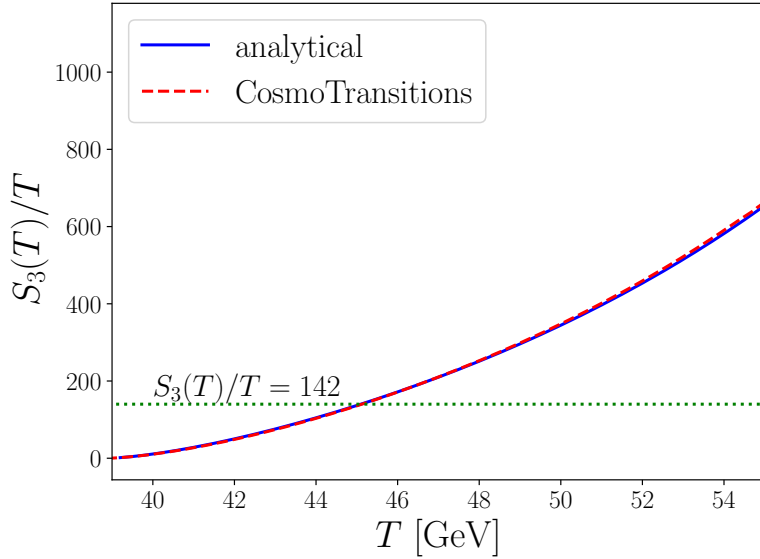


FIG. 13. $S_3(T)/T$ as function of temperature T for BP_1 .

Appendix B: thermal equilibrium

In the previous calculation, we have assumed that the DM has thermal equilibrium distribution in front of the bubble wall. This requires that the reflected DM should return to the same momentum as $p \sim T$ of the thermal plasma. In order to evaluate this, we have to evaluate the momentum exchange between reflected DM and DM in thermal equilibrium [44, 45].

In the false vacuum, the DM is massless. Some DM are reflected by bubble wall and will be out-of-equilibrium. By denoting the momentum of a particle in the plasma frame as $p^{\mathcal{P}} = (E^{\mathcal{P}}, p_x^{\mathcal{P}}, p_y^{\mathcal{P}}, p_z^{\mathcal{P}})$ with $E^{\mathcal{P}} = \sqrt{m_\chi^2 + (p_x^{\mathcal{P}})^2 + (p_y^{\mathcal{P}})^2 + (p_z^{\mathcal{P}})^2}$, the transformed momentum in the wall frame is

$$p = (E, p_x, p_y, p_z) = \left(\frac{E^{\mathcal{P}} + v_w p_z^{\mathcal{P}}}{\sqrt{1 - v_w^2}}, p_x^{\mathcal{P}}, p_y^{\mathcal{P}}, \frac{p_z^{\mathcal{P}} + v_w E^{\mathcal{P}}}{\sqrt{1 - v_w^2}} \right). \quad (\text{B1})$$

After DM reflects off the wall we have $p_z \rightarrow \tilde{p}_z = -p_z$, then the reflected momentum of DM in the plasma frame becomes

$$\tilde{p}^{\mathcal{P}} = \left(\tilde{E}^{\mathcal{P}}, \tilde{p}_x^{\mathcal{P}}, \tilde{p}_y^{\mathcal{P}}, \tilde{p}_z^{\mathcal{P}} \right) = \left(\frac{E + v_w p_z}{\sqrt{1 - v_w^2}}, p_x, p_y, \frac{-p_z - v_w E}{\sqrt{1 - v_w^2}} \right). \quad (\text{B2})$$

Then the $\tilde{E}^{\mathcal{P}}$ is given by

$$\tilde{E}^{\mathcal{P}} = \frac{(1 + v_w^2) E^{\mathcal{P}} + 2v_w p_z^{\mathcal{P}}}{1 - v_w^2}, \quad (\text{B3})$$

and $\tilde{p}_z^{\mathcal{P}}$

$$\tilde{p}_z^{\mathcal{P}} = -\frac{(1 + v_w^2) p_z^{\mathcal{P}} + 2v_w E^{\mathcal{P}}}{1 - v_w^2}, \quad (\text{B4})$$

from which the momentum exchange in a single collision of DM in the plasma frame is

$$\delta p_z^{\mathcal{P}} = \tilde{p}_z^{\mathcal{P}} - p_z^{\mathcal{P}} = -2v_w \frac{v_w p_z^{\mathcal{P}} + E^{\mathcal{P}}}{1 - v_w^2}. \quad (\text{B5})$$

The thermal plasma has $|\mathbf{p}^{\mathcal{P}}| \sim \mathcal{O}(T)$. The reflected χ and χ in thermal equilibrium has momenta

$$p_1^{\mathcal{P}} = (T + \frac{2v_w T}{(1 - v_w)T}, 0, 0, -T - \frac{2v_w T}{(1 - v_w)T}), \quad p_2^{\mathcal{P}} = (T, 0, 0, T) \quad (\text{B6})$$

respectively. The center-of-mass (CM) frame momentum is then

$$p_{\text{CM}}^{\mathcal{P}} = p_1^{\mathcal{P}} + p_2^{\mathcal{P}} = \left(\frac{2}{1 - v_w} T, 0, 0, \frac{-2v_w}{1 - v_w} T \right). \quad (\text{B7})$$

Hence, the velocity of the CM frame is $v_{\text{CM}} = -v_w$ and the Mandelstam variable \hat{s} of the scattering is

$$\hat{s} = 4T^2 \frac{1 + v_w}{1 - v_w}. \quad (\text{B8})$$

The elastic collision in the CM frame is represented as $p'_1 + p'_2 \rightarrow p'_3 + p'_4$ with

$$\begin{aligned} p'_1 &= (E_{\text{CM}}, 0, 0, -E_{\text{CM}}), & p'_2 &= (E_{\text{CM}}, 0, 0, E_{\text{CM}}), \\ p'_3 &= (E_{\text{CM}}, 0, -E_{\text{CM}} \sin \theta, -E_{\text{CM}} \cos \theta), & p'_4 &= (E_{\text{CM}}, 0, E_{\text{CM}} \sin \theta, E_{\text{CM}} \cos \theta). \end{aligned} \quad (\text{B9})$$

with $E_{\text{CM}} = p_{\text{CM}} = \sqrt{\hat{s}}/2$.

The momentum loss in such a collision in the plasma frame is

$$\delta p_{\chi} = p_{1z}^{\mathcal{P}} - p_{3z}^{\mathcal{P}} = \gamma_{\text{CM}} (p'_{1z} - p'_{3z}) = -\frac{\gamma_{\text{CM}} \hat{t}}{2E_{\text{CM}}}, \quad (\text{B10})$$

where we have Lorentz transformed between the CM and plasma frames and we use $\hat{t} = (p'_1 - p'_3)^2 = -2E_{\text{CM}}^2(1 - c_{\theta})$. Now we can derive the momentum-loss rate

$$\begin{aligned} \frac{d \log(p_{\chi})}{dt} &\approx \frac{n_{\chi} v_{\text{Mø1}}}{p_{\chi}} \int_{-4E_{\text{CM}}^2}^0 dt \frac{d\sigma}{d\hat{t}} \delta p_{\chi}, \\ &\approx -\frac{\gamma_{\text{CM}} n_{\chi} v_{\text{Mø1}}}{2E_{\text{CM}} T} \int_{-4E_{\text{CM}}^2}^0 dt \frac{d\sigma}{d\hat{t}} \hat{t}, \end{aligned} \quad (\text{B11})$$

where $v_{\text{Møl}} \simeq 2$ is the Møller velocity and

$$n_\chi = g_\chi \frac{3\zeta_3}{4\pi^2} T^3, \quad \frac{d\sigma}{d\hat{t}} = \frac{|i\mathcal{M}|^2}{16\pi\hat{s}^2} = \frac{y_\chi^4}{16\pi\hat{s}^2}. \quad (\text{B12})$$

Then the thermal equilibrium condition will be

$$\frac{d \log(p_\chi)}{dt} > H \rightarrow y_\chi \gtrsim 5.4 \times 10^{-4} \left(\frac{g_\star}{120}\right)^{1/8} \left(\frac{2}{g_\chi}\right)^{1/4} \left(\frac{T_n}{100 \text{ GeV}}\right)^{1/4} (1 + v_w)^{1/4} \quad (\text{B13})$$

Besides of this, we also require that the DM reflected off should be quickly annihilate away, then we have [2]

$$y_\chi \gtrsim (8 \times 10^{-4}) \left(\frac{T_n}{1\text{TeV}}\right)^{1/4} \left(\frac{g_\star}{120}\right)^{1/8} \left(\frac{\log 36T_n^2/m_\phi^2}{\log 36}\right)^{-1/4}. \quad (\text{B14})$$

- [1] G. Bertone and D. Hooper, *Rev. Mod. Phys.* **90**, 045002 (2018), 1605.04909.
- [2] M. J. Baker, J. Kopp, and A. J. Long, *Phys. Rev. Lett.* **125**, 151102 (2020), 1912.02830.
- [3] D. Chway, T. H. Jung, and C. S. Shin, *Phys. Rev. D* **101**, 095019 (2020), 1912.04238.
- [4] E. Krylov, A. Levin, and V. Rubakov, *Phys. Rev. D* **87**, 083528 (2013), 1301.0354.
- [5] F. P. Huang and C. S. Li, *Phys. Rev. D* **96**, 095028 (2017), 1709.09691.
- [6] D. Marfatia and P.-Y. Tseng, *JHEP* **02**, 022 (2021), 2006.07313.
- [7] M. Ahmadvand, *JHEP* **10**, 109 (2021), 2108.00958.
- [8] W. Chao, X.-F. Li, and L. Wang, *JCAP* **06**, 038 (2021), 2012.15113.
- [9] A. Azatov, M. Vanvlasselaer, and W. Yin, *JHEP* **03**, 288 (2021), 2101.05721.
- [10] M. J. Baker, M. Breitbach, J. Kopp, L. Mitnacht, and Y. Soreq, *JHEP* **08**, 010 (2022), 2112.08987.
- [11] A. Azatov, M. Vanvlasselaer, and W. Yin, *JHEP* **10**, 043 (2021), 2106.14913.
- [12] P. Huang and K.-P. Xie, *JHEP* **09**, 052 (2022), 2206.04691.
- [13] N. Aghanim et al. (Planck), *Astron. Astrophys.* **641**, A6 (2020), [Erratum: *Astron. Astrophys.* **652**, C4 (2021)], 1807.06209.
- [14] T. Hambye, A. Strumia, and D. Teresi, *JHEP* **08**, 188 (2018), 1805.01473.
- [15] C. L. Wainwright, *Comput. Phys. Commun.* **183**, 2006 (2012), 1109.4189.
- [16] F. C. Adams, *Phys. Rev. D* **48**, 2800 (1993), hep-ph/9302321.
- [17] J. Ellis, M. Lewicki, and J. M. No, *JCAP* **07**, 050 (2020), 2003.07360.

- [18] G. D. Moore and T. Prokopec, Phys. Rev. D **52**, 7182 (1995), hep-ph/9506475.
- [19] G. D. Moore and T. Prokopec, Phys. Rev. Lett. **75**, 777 (1995), hep-ph/9503296.
- [20] S. Jiang, F. P. Huang, and X. Wang (2022), 2211.13142.
- [21] M. Barroso Mancha, T. Prokopec, and B. Swieczewska, JHEP **01**, 070 (2021), 2005.10875.
- [22] W.-Y. Ai, B. Garbrecht, and C. Tamarit, JCAP **03**, 015 (2022), 2109.13710.
- [23] S. Balaji, M. Spannowsky, and C. Tamarit, JCAP **03**, 051 (2021), 2010.08013.
- [24] D. Bodeker and G. D. Moore, JCAP **05**, 009 (2009), 0903.4099.
- [25] Y. Gouttenoire, R. Jinno, and F. Sala, JHEP **05**, 004 (2022), 2112.07686.
- [26] S. H"ocher, J. Kozaczuk, A. J. Long, J. Turner, and Y. Wang, JCAP **03**, 009 (2021), 2007.10343.
- [27] J. R. Espinosa, T. Konstandin, J. M. No, and G. Servant, JCAP **06**, 028 (2010), 1004.4187.
- [28] C. Caprini and J. M. No, JCAP **01**, 031 (2012), 1111.1726.
- [29] B. Laurent and J. M. Cline, Phys. Rev. D **106**, 023501 (2022), 2204.13120.
- [30] L. Leitao and A. Megevand, Nucl. Phys. B **891**, 159 (2015), 1410.3875.
- [31] F. Giese, T. Konstandin, and J. van de Vis, JCAP **07**, 057 (2020), 2004.06995.
- [32] X. Wang, F. P. Huang, and X. Zhang, Phys. Rev. D **103**, 103520 (2021), 2010.13770.
- [33] E. Witten, Phys. Rev. D **30**, 272 (1984).
- [34] C. J. Hogan, Mon. Not. Roy. Astron. Soc. **218**, 629 (1986).
- [35] M. Kamionkowski, A. Kosowsky, and M. S. Turner, Phys. Rev. D **49**, 2837 (1994), astro-ph/9310044.
- [36] M. Hindmarsh, S. J. Huber, K. Rummukainen, and D. J. Weir, Phys. Rev. D **96**, 103520 (2017), [Erratum: Phys.Rev.D 101, 089902 (2020)], 1704.05871.
- [37] P. Amaro-Seoane et al. (LISA) (2017), 1702.00786.
- [38] J. Luo et al. (TianQin), Class. Quant. Grav. **33**, 035010 (2016), 1512.02076.
- [39] Z.-C. Liang, Z.-Y. Li, J. Cheng, E.-K. Li, J.-d. Zhang, and Y.-M. Hu, Phys. Rev. D **107**, 083033 (2023), 2212.02852.
- [40] W.-R. Hu and Y.-L. Wu, Natl. Sci. Rev. **4**, 685 (2017).
- [41] V. Corbin and N. J. Cornish, Class. Quant. Grav. **23**, 2435 (2006), gr-qc/0512039.
- [42] N. Seto, S. Kawamura, and T. Nakamura, Phys. Rev. Lett. **87**, 221103 (2001), astro-ph/0108011.
- [43] H. Kudoh, A. Taruya, T. Hiramatsu, and Y. Himemoto, Phys. Rev. D **73**, 064006 (2006), gr-qc/0511145.

[44] K. Kawana, P. Lu, and K.-P. Xie, JCAP **10**, 030 (2022), 2206.09923.

[45] I. Baldes, Y. Gouttenoire, and F. Sala, SciPost Phys. **14**, 033 (2023), 2207.05096.